

1 Impact of boundary layer stability on urban park
2 cooling effect intensity

3

4 *Authors: Martial Haeffelin¹, Jean-François Ribaud², Jonnathan Céspedes², Jean-*
5 *Charles Dupont³, Aude Lemonsu⁴, Valéry Masson⁴, Tim Nagel⁴, Simone Kotthaus²*

6

7 *¹ Institut Pierre Simon Laplace (IPSL), CNRS, Ecole polytechnique, Institut Polytechnique de Paris, 91128*
8 *Palaiseau Cedex, France*

9 *² Laboratoire de Météorologie Dynamique (LMD-IPSL), Ecole polytechnique, Institut Polytechnique de*
10 *Paris, 91128 Palaiseau Cedex, France*

11 *³ Institut Pierre Simon Laplace (IPSL), Université Versailles Saint-Quentin-en-Yvelines, 78240*
12 *Guyancourt, France*

13 *⁴ Centre national de recherches météorologiques (CNRM), Université de Toulouse, Météo-France,*
14 *CNRS, Toulouse, France*

15

16 Correspondence to: Martial Haeffelin (martial.haeffelin@ipsl.fr)

17 Abstract

18 The added heat in cities amplifies the health risks of heat waves. At night under calm winds
19 and cloud free skies, the air in the urban canopy layer can be several degrees warmer than in
20 rural areas. This lower nocturnal cooling in the built-up settings poses severe health risks to
21 the urban inhabitants as indoor spaces cannot be ventilated effectively. With heat waves
22 becoming more frequent and more intense in future climates, many cities are expanding their
23 green spaces with the aim to introduce cooling through shading, evaporation, and lower heat
24 storage capacities. In this study, it is assessed how the evening and night-time cooling effect
25 of urban parks (relative to nearby built-up settings) varies with the park size and the meso-
26 scale atmospheric conditions during warm summer periods. Using a combination of
27 meteorological surface station data and compact radiosondes, the cooling effect is quantified
28 for several urban parks (about 15 ha) and urban woods (about 900 ha). A profiling Doppler
29 wind lidar deployed in the city centre is used to measure turbulent vertical mixing conditions
30 in the urban boundary layer. We find that the maximum nocturnal cooling effects in urban
31 parks range around 1-5°C during a one-week heat wave event in mid-July 2022 but also in
32 general during summer 2022 (June-August). Three atmospheric stability and mixing regimes
33 are identified that explain the night-to-night variability in park cooling effect. We find that
34 very low turbulent vertical mixing in the urban boundary layer ($< 0.05 \text{ m}^2\text{s}^{-2}$) results in the
35 strongest evening cooling in both rural settings and urban parks and the weakest cooling in
36 the built-up environment. This regime specifically occurs during heat waves in connection
37 with large-scale advection of hot air over the region and corresponding subsidence. When
38 nocturnal turbulent vertical mixing above the city is stronger, the evening cooling in urban
39 green spaces is less efficient so that the atmospheric stratification above both urban parks
40 and woods is less stable and temperature contrasts compared to the built-up environment
41 are less pronounced. These results highlight that urban green spaces have a significant cooling
42 potential during heat waves, with maximum effects at night as advection and mixing transport
43 processes are minimal. This suggests adapting the opening hours of public parks to enable
44 residents to benefit from these cooling islands.

45

46 1 - Introduction

47 Excess heat in cities has impacts on human comfort, labour productivity, and health. Mortality
48 has been linked to exceptionally high temperatures during summertime heat waves both at
49 night and during the day (Basu et al. 2002; Keatinge et al. 2000; Pirard et al. 2005). During the
50 day, it is the outdoor radiative temperature that poses the most significant health risk. At
51 night, indoor temperatures are particularly important as people need to rest and indoor air
52 must be vented to cool the building for the upcoming day. However, urban inhabitants can
53 be particularly exposed to excessive and prolonged heat stress at night as the city and the
54 buildings do not cool efficiently, preventing necessary nocturnal rest. Hot nights following hot
55 days have been shown to make an important contribution to heat-related mortality (Murage
56 et al. 2017; Royé et al., 2021).

57

58 Reducing people's exposure to heat in cities can be addressed through urban planning
59 strategies. Increasing the vegetation fraction of urban areas is a widely accepted strategy to
60 mitigate urban heat risk by effectively reducing heat storage uptake during daytime
61 (Grimmond and Oke, 2002). Trees can provide efficient shading, reducing daytime air
62 temperatures by several degrees below their canopy, while evapotranspirative cooling
63 provided by vegetation, including trees, shrubs and grass, maintain the green space
64 temperature several degrees below that of the built-up environment (Shashua-Bar and
65 Hoffman, 2000). Green infrastructures also show cooling effects at night, through continued
66 evapotranspiration after sunset, generally larger sky-view factors in urban parks than in built-
67 up environments, and lower heat capacities. However, reduced radiative cooling and
68 ventilation can retain heat below the canopy at night (Taha et al. 1991).

69

70 The cooling effect intensity of urban green infrastructure has been shown to be highly variable
71 (Bowler et al. 2010; Shoulika et al 2014). Doick et al (2014) point to a lack of certainty on the
72 variables that drive the park cooling effects and on the multiple roles of trees and
73 greenspaces. Spatial contrasts in nocturnal temperatures between green infrastructure and
74 nearby built-up areas depend on park perimeter and area (Gao et al. 2022; Cai et al. 2023),
75 on proportion of grass and trees, on tree size (Zhu et al. 2021), on vegetation types and
76 arrangements (street trees vs parks), on density of vegetation (Holmer et al 2013), on park

77 topography (Barradas 1991; Chang et al. 2007), and on local climates (Ibsen et al. 2021). Other
78 authors investigated the spatial extent of cooling by urban parks, i.e. the *cooling effect*
79 *distance*, showing that it depends on both park size and park greenness (e.g. Zhu et al 2021).
80 From a recent review of park cooling effect studies conducted by Aram et al. (2019), we
81 conclude that most studies focus on the impact of park characteristics and investigations on
82 the impact of meteorological conditions on park cooling effects are rare.

83

84 The impact of meteorological conditions, such as cloudiness, wind and turbulence on
85 differential cooling is studied mostly at regional scale in terms of their impact on the urban
86 heat island (UHI) intensity (Oke 2017). While the influence of cloud cover and wind is rather
87 established (e.g. Morris et al. 2001, Lin et al. 2022), also the occurrence and characteristics of
88 night-time low-level jets are found to influence UHI intensity (Lemonsu et al. 2009; Cespedes
89 et al. 2024). However, the impact of local- to meso-scale meteorological phenomena on
90 cooling effects of urban green infrastructure is not well quantified.

91

92 The combined effects of green infrastructure characteristics and meteorological regimes on
93 nocturnal cooling must hence be better understood so that the cooling effect of urban
94 renaturation projects can be quantified more precisely. Which conditions affect the park
95 cooling effect intensity? What is the relative impact of park characteristics and meteorological
96 processes in the urban boundary layer on the cooling intensity ?

97

98 The overall objective of this study is to quantify in detail the nocturnal cooling effects of urban
99 parks during warm summertime conditions, taking into account potential cooling effects from
100 the rural surroundings. We carried out this study in the framework of the Heat and Health in
101 Cities project (H2C, Lemonsu et al. 2024) that focuses on the effects of excessive summertime
102 heat and air pollution on human vulnerability (Forceville et al. 2024) with the Paris region
103 (France) as a study area. A dedicated field campaign was designed and carried out in the city
104 of Paris and the surrounding region to monitor spatial and temporal variations in key
105 atmospheric thermodynamic variables in the urban canopy layer and urban boundary layer
106 during summer 2022. The measurements performed, including near-surface and vertical
107 profiles of temperature, humidity, wind and turbulence, and data analysis methodology are
108 presented in Section 2. Section 3 presents the analysis of urban park cooling effects in relation

109 to regional UHI and their variability during summer 2022, with a focus on a one-week heat
110 wave event. Next (Section 4), we investigate the characteristics of the urban boundary layer
111 structure under three distinct atmospheric turbulence regimes and their influence on park
112 cooling effects. Finally, we quantify the role of atmospheric stability and vertical turbulent
113 mixing on differential evening cooling between built-up locations, urban parks and rural
114 settings (Section 5).

115

116 2 - Data and methodologies

117 The present study is based upon data collected in the Paris region during the first Special
118 Observation Period of the Heat and Health in Cities project (SOP 2022, Figure 1), which was
119 conducted during summer 2022. This campaign also benefited from measurements carried
120 out in the context of other research initiatives such as the Paris 2024 Olympics WMO Research
121 and Development Project (RDP-2024) and the ACTRIS research infrastructure (Laj et al. 2024).
122 This multi-project context motivated the pooling of resources, a coordinated strategy for the
123 organisation of the summer-2022 experimental campaigns, and the development of a joint
124 data repository under the name PANAME (PARis region urbaN Atmospheric observations and
125 models for Multidisciplinary rEsearch - see <https://paname.aeris-data.fr/>).

126

127 2.1 Datasets used in the study

128 This study combines continuous measurements collected from June to August 2022 and 14
129 one-day intensive observation periods (IOPs), with data collected from mid-June to the end
130 of July 2022. Measurement locations are shown in Figure 1.

131

132 i) Surface meteorological stations

133 Météo France's operational network consists of some fifty ground-based weather stations in
134 the Paris region measuring at least air temperature at 2 m AGL with a 6-minute acquisition
135 time step. A few stations provide additional meteorological parameters such as wind speed
136 and direction at 10 m AGL, global incoming radiation, precipitation, and cloud cover. The

137 stations are spread across the region in different areas, but are always installed on the ground
138 on an open lawn (according to WMO recommendations).

139

140 We selected six stations to represent rural settings (Local Climate Zone, Stewart and Oke
141 2012) of the Paris region (Figure 1), located in Changis, Courdimanche, Fresnoy-La-Riviere,
142 Maule, Melun, and Pontoise, which is similar to the stations selected by Lemonsu et al. (2015).
143 The stations are geographically distributed in all directions relative to the city centre of Paris
144 and located at altitudes ranging 50-90 m above sea level (ASL). In our study, the reference
145 rural setting conditions of temperature, wind speed and direction are computed as the
146 average of the variables measured at those six stations (Changis, Courdimanche, Melun, and
147 Pontoise stations).

148

149 Near-surface urban park weather conditions are documented by a Météo-France weather
150 station located in the Montsouris Park, a 15-ha park located in the 14th district, south of the
151 Paris city centre. The station, located at an elevation of 75 m ASL, provides 2-m air
152 temperature and humidity measurements. Wind speed and direction are measured at 25 m
153 above ground level (AGL). A detailed description of temperature measurements in the
154 Montsouris Park is provided by Dahech et al. (2020).

155

156 The Paris built-up setting conditions are sampled using Internet of Things (IoT) temperature
157 and humidity measurements. This compact technology opens up new perspectives in
158 meteorological measurements, particularly in urban environments where measurement and
159 installation conditions are sometimes complicated. More than twenty IoT stations (DecentLab
160 DL-SHT35-001 - air temperature and humidity sensor with radiation shield for LoRaWAN) have
161 been installed in central Paris starting in July 2022. These are compact and lightweight
162 stations installed on lampposts at a height of approximately 5 m AGL, following the
163 recommendations made by Oke (2006). The stations have been installed on the north side of
164 the lampposts to limit sensor warming through solar irradiance. The reference built-up setting
165 temperature is computed as the average temperature recorded by four IoT stations located
166 within 500 m of each other, in the highly urbanised neighbourhood of the Paris Opera House
167 (hereafter referred to as Opera). Note that these stations were operational only from July 8,
168 2022. For the period prior to this date (1 June to 7 July), the built-up setting temperature is

169 derived from the Météo France weather station Lariboisière Hospital (10th district of Paris)
170 which is located 2 km northeast of the Opera neighbourhood in an equally dense built-up
171 setting. Comparisons of temperatures measured at Lariboisière and Opera during July and
172 August 2022 do not reveal any significant differences (not shown). The built-up setting
173 temperature (at Lariboisière and Opera) is considered not influenced by green space cooling,
174 as the closest urban park is about 1 km away and cooling effect distances of parks reported
175 in the literature are far less than 1 km (Aram et al. 2019).

176

177 Finally, we used temperature and wind speed and direction measured at the top of the Eiffel
178 Tower (287 m AGL) to monitor conditions at a height generally located in the nocturnal urban
179 boundary layer.

180

181 **i) Doppler Wind Lidar**

182 A Doppler Wind Lidar (DWL) is used in this study to deduce the intensity of vertical turbulent
183 mixing. The Vaisala DWL WindCube Scan 400 was installed at 90 m above ground level (AGL)
184 at the top of the Zamansky Tower located on the campus of Sorbonne University in the 5th
185 district of Paris (QUALAIR atmospheric station location shown on Fig. 1; <https://qualair.fr/>) to
186 measure horizontal wind and vertical velocity. In this study, we use vertical-stare mode of the
187 DWL to derive vertical velocity variance (σ_w) profiles. Each variance profile is calculated from
188 300 vertical velocity profiles collected during a 5-min period (one profile per second). Vertical
189 velocity variance profiles are available every 30 minutes. Due to the installation setup, the
190 first gate available for deriving the vertical velocity variance is at 240 m AGL.

191

192 **ii) Windsond**

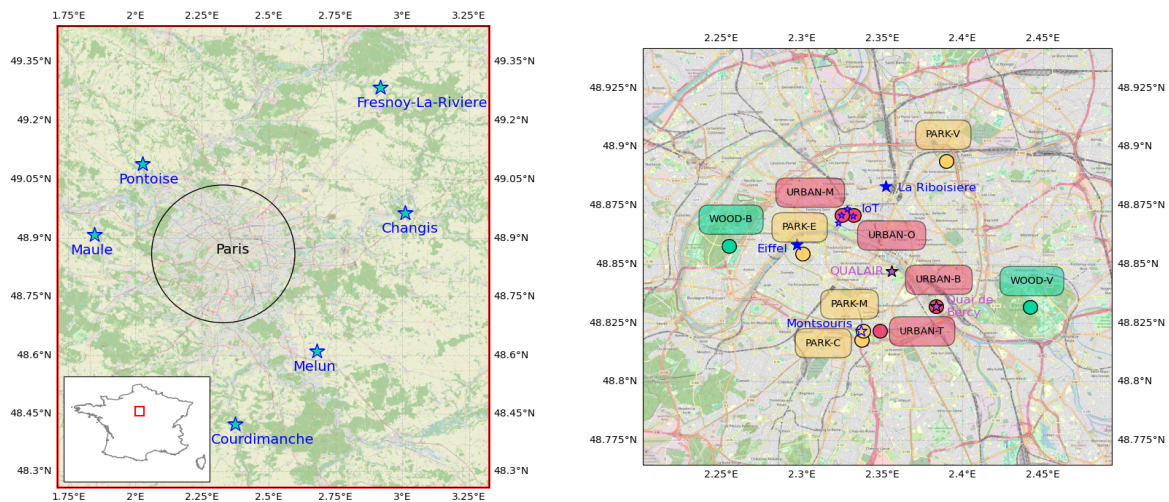
193 A Windsond is a lightweight sonde (12 grams) manufactured by Sparv Embedded, Sweden
194 (<https://sparvembedded.com/products/windsond>). This instrument, packaged in a styrofoam
195 cup, records pressure, temperature, and relative humidity approximately every second.
196 Latitude and longitude are determined using an onboard GPS receiver. The S1H3 windsond
197 model calculates wind speed and direction independently from latitude and longitude,
198 utilising the GPS signal. Thanks to its lightweight design, the balloon size is somewhat

199 equivalent to a "party balloon", requiring about 50 L of helium, and making it particularly
200 suitable for probing the lower parts of the troposphere.

201 For each IOP, three profiles were produced using windsonds to monitor evening cooling at
202 16, 20 and 00 UTC. The 16 UTC profile corresponds to conditions of maximum daytime
203 temperatures. The 20 UTC profile samples conditions about 1 hr after sunset, while the 00
204 UTC profile is performed in conditions close to the maximum nighttime UHI.

205 Corrections have been applied to raw data as follows. Before the windsond is released, the
206 temperature and humidity sensors are not ventilated. Unventilated data (before launch) are
207 thus carefully compared with the first points of the ventilated profile, and corrected if
208 necessary. As the temperature and humidity sensors are outside the styrofoam cup, the
209 windsond is subject to the influence of solar radiation during the day. A daytime overheating
210 on the order of about +1°C was observed by comparing those profiles with data collected by
211 Vaisala RS41-SGP radiosondes launched at the same time the URBAN-B location (see
212 Appendix 1). A correction of -1°C was therefore applied across the entire profile for
213 windsonde data at 16 UTC. No radiative correction is applied at 20 and 00 UTC.

214



215

216 Figure 1: (left) Locations of the six weather stations contributing to the rural setting
217 reference. (right) Locations of fixed weather stations in Paris city (blue stars) and of
218 windsonde and radiosonde launch sites in urban woods (green dots WOOD), urban
219 parks (yellow dots PARK) and built-up areas (red dots URBAN). © OpenStreetMap
220 contributors 2023. Distributed under the Open Data Commons Open Database
221 License (ODbL) v1.0.

222

223
224

225 2.2 Sampling methodology

226

227 Our study focuses on evening temperature evolution at various locations across the Paris
228 region under predominantly cloud free conditions. The cloud cover fraction is derived on an
229 hourly basis using a Lufft CHM15k automatic lidar ceilometer located at the SIRTA observatory
230 (Haeffelin et al. 2005) and a second one located at the QUALAIR atmospheric station. Evening
231 cloud-free conditions are defined as a cloud fraction less than 20% for each hour between 16
232 and 00 UTC. In the period June-August 2022, 54 days are classified as “evening cloud-free
233 conditions”. On average this period is characterized by a positive temperature anomaly and
234 near-zero precipitation anomaly (not shown).

235

236 The 14 intensive observation days were selected to focus predominantly on warm to hot
237 daytime conditions followed by cloud free nights. Two heat wave events were covered with
238 intensive observations, the first one on 16-18 June and the second one on 12-19 July.

239 Windsond launch sites were classified in three types of settings i.e., urban woods, urban parks
240 and built-up areas. Two urban woods, located East of the city (Bois de Vincennes, 995 ha;
241 WOOD-V in Fig. 1) and West of the city (Bois de Boulogne, 845 ha; WOOD-B), are mostly
242 wooded, including open lawns, small lakes, buildings and roads. Three urban parks of
243 comparable size were selected to sample different neighbourhoods of the city. One is located
244 south of the city centre (Cité Universitaire about 32 ha with 50% green space and 50%
245 housings and small roads, located across the street from Montsouris Park; PARK-C), the
246 second one is West of the city centre (Eiffel Tower park, 24 ha, predominantly trees and open
247 lawns; PARK-E), and the third one is Northeast of the city centre (La Villette Park, 55 ha
248 including 30 ha of green space and 25 ha of built-up areas; PARK-V). The three selected urban
249 parks differ however in terms of vegetation type (species; fractions of trees, shrubs and grass)
250 and also in terms of irrigation practices and hence soil moisture. These differences and their
251 effects are not accounted for in this study. Windsonds were also launched from four built-up
252 areas: one in the 13th district close to Montsouris Park (URBAN-T in Fig 1.), two in the 9th
253 district close to the Opera IoT stations (URBAN-M and URBAN-O), and one in the 12th district

276 sites - see detailed definition of locations in Section 2). As park cooling effect intensity is
277 reported to be highly variable, we study this variability as a function of the nocturnal UHI in
278 the Paris region, which represents the regional-scale temperature contrasts between the
279 same built-up environment and the vegetated rural reference. The study covers summer 2022
280 focusing on the 54 evening periods with cloud-free conditions (defined in Section 2).
281

282 3.1 Summertime urban park cooling effect variability

283 The regional UHI is known to be dependent on both cloud-cover fraction and wind speed.
284 Here we focus on cloud-free nights, for which the UHI has been found to be proportional to
285 the inverse of the square-to-third root of the wind speed (e.g. Morris et al. 2001). Cespedes
286 et al. (2024) has also shown that the strongest UHI intensities are found for very low vertical
287 velocity variance values, measured above the urban canopy, and that UHI decreases as
288 vertical velocity variance increases.

289 Fig. 2 presents median nocturnal cooling intensity of the Montsouris Park (a 15-ha urban park)
290 against the median nocturnal regional UHI and median vertical velocity variance computed
291 over the 19-02 UTC time interval for each night. A K-means clustering method based on the
292 three variables is used to identify different regimes. The figure reveals three different
293 regimes. In conditions of strongest UHI (6-10°C), we find a group of days where the park
294 cooling effect intensity ranges 2-5°C. In this regime, the vertical velocity variance is very low
295 with median nocturnal values ranging from 0.02 to 0.1 m²s⁻². In these conditions, urban park
296 cooling intensity relative to the built-up environment shows a strong variability, but is on
297 average half the regional UHI intensity. In conditions of weak UHI intensity (2-4°C), the park
298 cooling effect is close to 1°C, while the vertical velocity variances are high (greater than 0.25
299 m²s⁻²). In this regime, intra-urban temperatures are most homogeneous and urban-rural
300 contrasts are minimal, which is likely due to significant advection. In between, we find a
301 number of days where the urban park cooling effect remains limited (1-2°C), while the urban-
302 rural temperature contrasts are significantly stronger (4-8°C), by a factor of about four. In
303 these conditions, we find that the vertical velocity variances range between 0.1 and 0.2 m²s⁻².
304 For those days, the rural environment around the city cools very efficiently, while the urban
305 setting remains hot with little intra-urban contrasts.

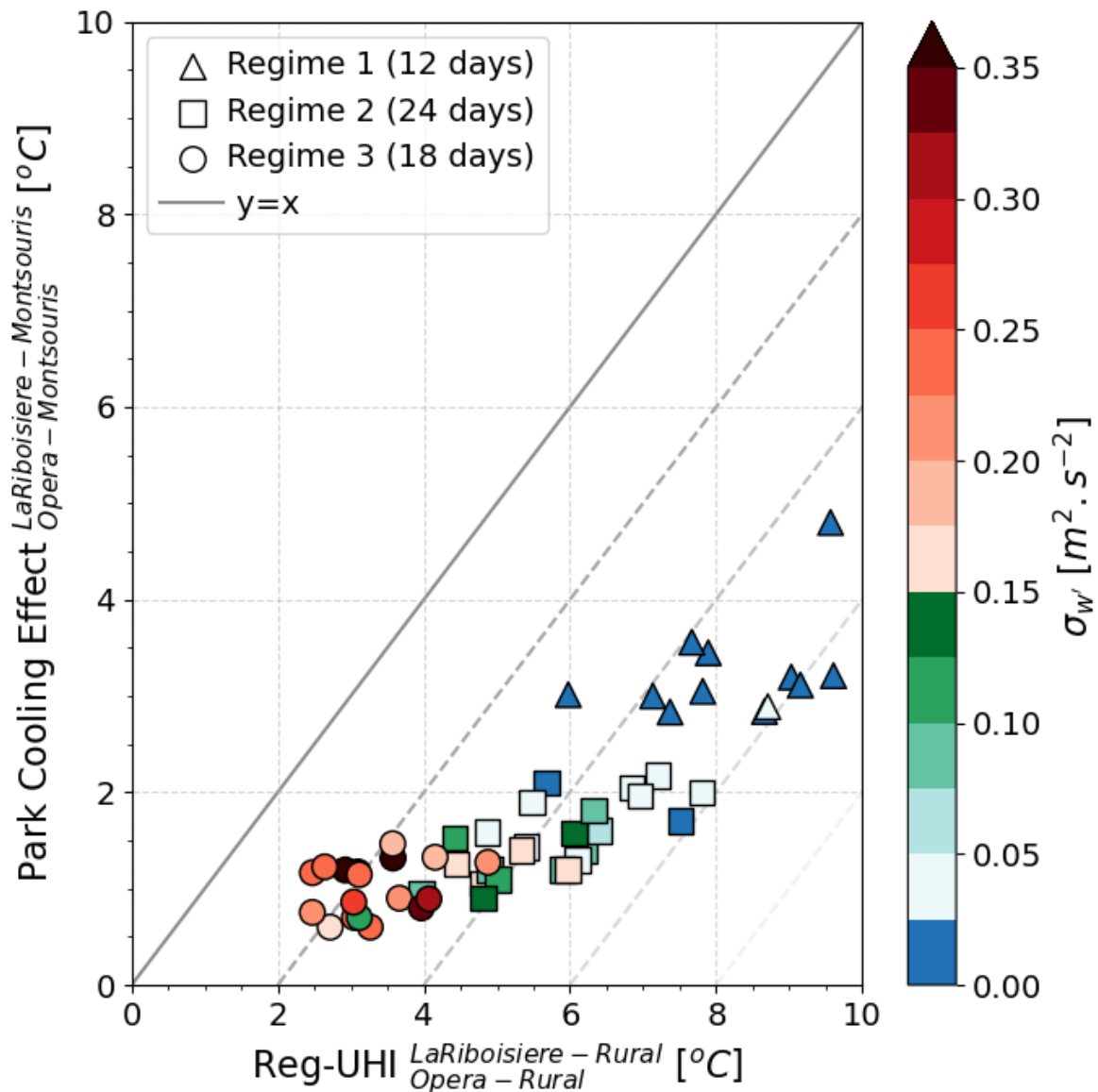
306 In summary, we can state that:

- 307 ● Conditions of strong park cooling intensity combined with strong regional UHI
308 intensity occur in a regime of low vertical velocity variance. This regime will be referred
309 to as the stagnant regime in the rest of the paper,
- 310 ● Conditions of moderate park cooling intensity combined with strong regional UHI
311 intensity occur in a regime of moderate vertical velocity variance (referred to as the
312 intermediary regime).
- 313 ● conditions of weak park cooling intensity combined with weak regional UHI intensity
314 occur in a regime of high vertical velocity variance (referred to as the turbulent
315 regime).

316 Based on these findings, several questions arise. What processes drive the evening cooling in
317 the urban park in these different conditions? What is responsible for the different urban park
318 cooling effects that we find for low, moderate and high vertical velocity variance?

319

320



321
 322 Figure 2. Nocturnal urban park cooling effect intensity against regional-scale UHI intensity and
 323 vertical velocity variance (color scale), derived from 8 hours of measurements (median 19-02
 324 UTC values) for the 54 cloud-free evenings.

325

326 3.2 Urban park cooling effect variability in a heatwave period

327

328 To better understand factors affecting the variability in nocturnal temperature contrasts
 329 between urban parks and the built-up settings, we focus next on an eight-day event (12-19

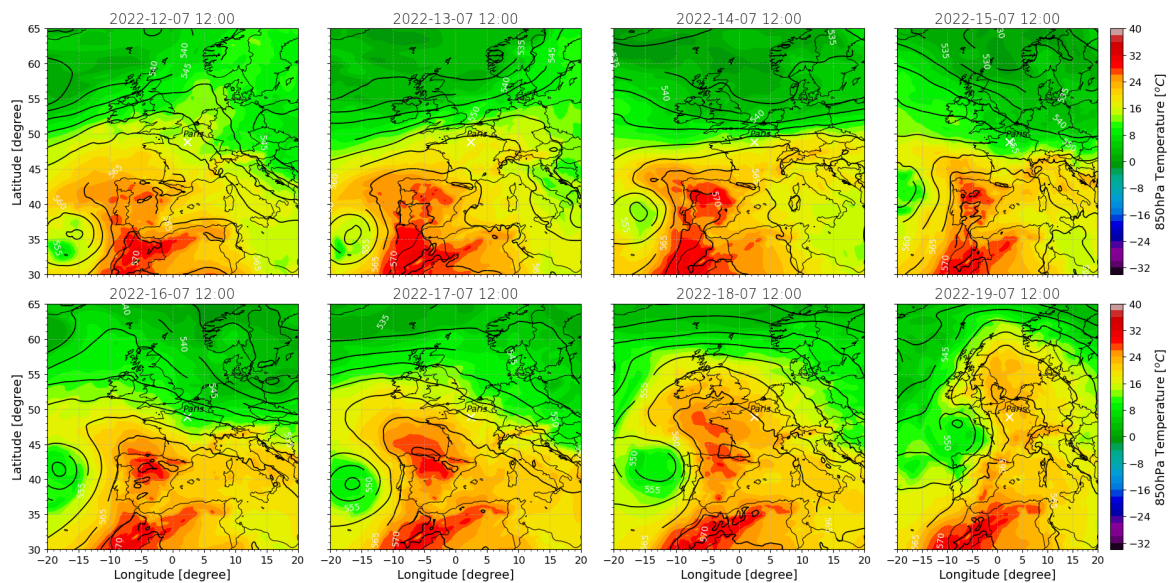
330 July 2022) that is characterised by extreme daytime temperature (peak values approaching
331 40°C on several days) and a set of diverse evening cooling patterns.

332

333 This period is characterised by a powerful anticyclonic axis between Morocco, France and the
334 British Isles, which gradually warmed the air (Fig. 3). A secondary low-pressure system located
335 between the Azores and Portugal moved towards the Bay of Biscay, strengthening advection
336 of particularly hot air from the Iberian Peninsula. This contributed to the intensification of a
337 heatwave over the European continent, with an extreme peak over the Paris region on 19
338 July. As it moved north-eastwards over France, this low pressure system advected cooler
339 oceanic air from the west, causing temperatures to fall and progressing eastwards with
340 thunderstorm activity. During the heatwave, the 850 hPa temperature exceeded 20°C, while
341 on standard summer days, it is closer to 10°C.

342

343



344

345 Figure 3: Synoptic overview from 12 to 19 July 2022 based on ERA5 reanalysis. The colour
346 bar represents temperature at 850 hPa, and the contours represent the geopotential height
347 difference between 500 hPa and 1000 hPa (dam).

348

349 Figure 4 shows the temporal evolution of near-surface atmospheric conditions during the
350 eight-day period. Figure 4a compares the 2-m air temperature measured in Opera built-up
351 setting, Montsouris urban park, and the rural reference setting. The regimes identified in
352 Section 3.1 are also shown for each night. Figure 4b presents the rate of change of

353 temperature over time at the three locations. Figure 4c shows the temperature differences
354 between the built-up site and the urban park and the rural setting, respectively. Figure 4d
355 presents the wind speed and direction measured at the Montsouris urban park 25 m AGL and
356 Fig. 4e shows the vertical velocity variance measured at 240 m AGL.

357

358 The eight-day period is characterised by a first heat wave on July 12 and 13 (stagnant regime),
359 due to the advection of hot air shown in Fig. 3, with maximum temperature exceeding 35°C,
360 followed by three days of more moderate heat on July 14, 15, and 16 (intermediary and
361 turbulent regimes, maximum temperature at or below 30°C and minimal temperatures in the
362 built-up environment less than 20°C). A second, more intense, advection of hot air occurs the
363 following three days on July 17, 18, and 19 (stagnant regime) with daytime maximum
364 temperatures exceeding 35°C. Figure 4a shows that the daytime maximum temperatures
365 (between 16 and 17 UTC) in the built-up, urban park and rural settings are close, within 1°C
366 of each other. Conversely, night-time minimal temperatures (between 03 and 04 UTC) differ
367 by 4-10°C between the built-up and rural settings with significant day to day variations (Figure
368 4c).

369

370 Figure 4b shows positive heating rates from sunrise until about one hour before sunset. Peak
371 heating rates reach 2-3°C/hr, but are on average near 1°C/hr. One hour before sunset,
372 temperature changes become negative (cooling). We observe a two-phase cooling consistent
373 with earlier findings reported in the literature (e.g. Holmer et al. 2013). The first phase lasts
374 from 16 to 21 UTC. It is characterised by large changes in cooling rate reaching maximum
375 values near 19-20 UTC and with differences of up to 2°C/hr between built-up, urban park, and
376 rural cooling rates (on 12/07, 17/07 and 18/07). The second phase starts after 21 UTC and
377 lasts until sunrise or about 04 UTC. It is characterised by more moderate cooling rates of
378 typically less than -1°C/hr and by virtually no contrasts between built-up, park and rural
379 settings.

380

381 In the evening, air temperature cooling in the urban canopy is driven by a combination of
382 processes, including radiative cooling of the surfaces and the air (through radiative flux
383 divergence), turbulent heat exchange (through sensible and latent heat fluxes), release of
384 heat from the ground (storage heat flux), vertical mixing of air, and advection (Oke 2017).

385 These processes are known to depend on the surface types and properties (albedo, emissivity,
386 heat capacity, soil moisture), the 3-D canopy structure (sky view factor), the city morphology,
387 anthropogenic heat emissions, the spatial distribution of surface types (urban to rural surface
388 gradients), and synoptic-scale weather conditions (wind, clouds). According to Steeneveld et
389 al. (2006), atmospheric static stability and mesoscale dynamics affect the relative contribution
390 of the radiative and turbulent processes. When the vertical turbulent mixing is low, turbulent
391 heat fluxes are weak, hence air temperature cooling is dominated by radiative flux divergence,
392 partially compensated by the storage heat flux.

393

394 This is consistent with cooling rates shown in Fig. 4b. In the rural setting and in the urban park,
395 where the storage heat flux is low, the largest cooling rates (peaking at $-3^{\circ}\text{C}/\text{hr}$ and $-2^{\circ}\text{C}/\text{hr}$
396 respectively) are observed in conditions of low vertical velocity variance (Fig. 4e), on the
397 evenings of 12/07, 17/07 and 18/07 (stagnant regime). In the built-up area, the radiative
398 cooling is partially compensated by a stronger ground heat flux. On nights with moderate to
399 high vertical velocity variance, radiative flux divergence is reduced and also compensated by
400 sensible and latent heat flux releases, which leads to lower cooling rates in both urban park
401 and rural settings. The excess of urban-park cooling compared to the built-up environment
402 lasts four to six hours (from 18 to 00 UTC) as is the case for the rural surface.

403

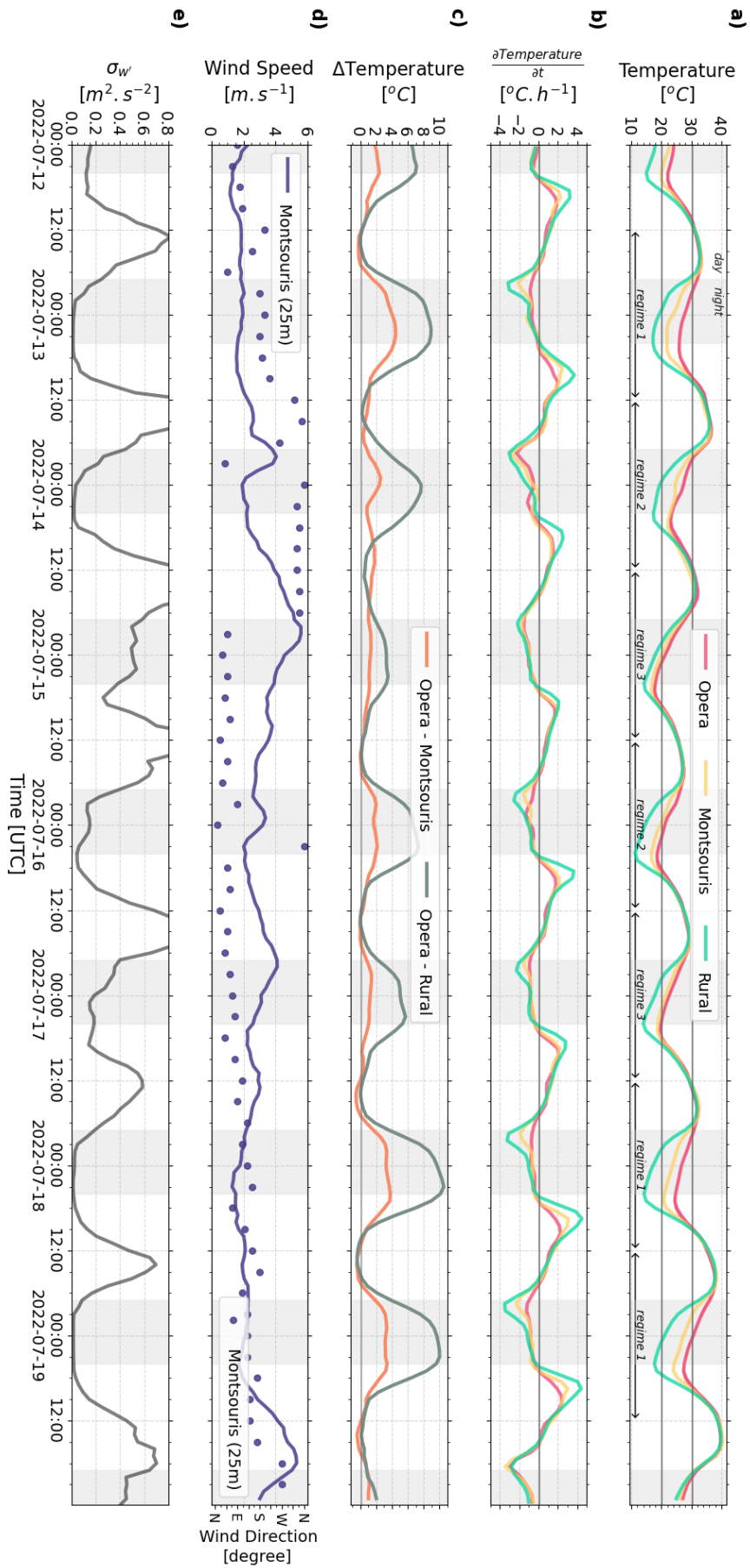
404 The contrasts in cooling rates between the built-up environment, the urban park and the rural
405 settings can explain the large variability in nocturnal park cooling effect and regional-scale
406 UHI intensities shown in Fig. 4c. On the three nights with lowest wind speed ($<2\text{ m s}^{-1}$, Fig. 4d)
407 and lowest vertical velocity variance ($<0.05\text{ m}^2\text{ s}^{-2}$), that is on 12-13/07, 17-18/07 and 18-
408 19/07 (stagnant regime), the maximum regional UHI intensity exceeds 8°C , while the
409 maximum park cooling effect reaches nearly 4°C . On those nights, in the built-up
410 environment, the air temperature cools by $7\text{-}9^{\circ}\text{C}$ from sunset to sunrise, while the urban park
411 cools an extra $3\text{-}4^{\circ}\text{C}$, and the rural setting an additional $3\text{-}4^{\circ}\text{C}$. On the night with moderate
412 wind speed ($3\text{-}4\text{ m s}^{-1}$) and moderate vertical velocity variance, 15-16/07(intermediary
413 regime), the regional UHI peaks near 6°C , while the park cooling effect reaches about 2°C . On
414 this night, the air temperature cools by about 10°C from sunset to sunrise in the built-up
415 environment, while the urban green infrastructure cools an extra 2°C , and the rural setting an
416 additional $3\text{-}4^{\circ}\text{C}$. On the nights of 14-15/07 and 16-17/07 (turbulent regime), the wind speed

417 exceeds 4 m s^{-1} and the park cooling effect reaches just 1°C , while the maximum regional UHI
418 intensity is about 4°C .

419

420 The analysis of the 12-19 July period confirms the results shown in Fig. 2. Different regimes
421 exist that influence park cooling effect and regional UHI intensities. In particular, during nights
422 with very low wind speeds, the air above the urban park cools significantly more (up to 4°C)
423 than in our reference built-up environment. To better understand the processes and
424 conditions that affect these nocturnal intra-urban cooling contrasts we will investigate the
425 dynamics and thermodynamics of the urban boundary layer over green infrastructures of
426 different sizes in the following section.

427



429 Figure 4: near-surface temperature and nighttime turbulence regimes (a) and cooling rate (b)
430 measured in a built-up environment (Paris Opera district), an urban park (Montsouris park,
431 15-ha), and the average of 6 rural locations around Paris; Urban park cooling effect (Opera-
432 Montsouris temperature difference) and regional-scale UHI (Opera-Rural temperature
433 difference) (c); wind speed and direction measured at Montsouris Park 25 m AGL (d); and
434 vertical velocity variance measured in Paris city centre 240 m AGL. 12-19 July 2022; during
435 that week, the sun sets at about 19 UTC and rises at about 04 UTC.
436

437 4) Evening cooling in and above urban parks and 438 urban woods

439
440 In this section, we focus on four different nights to study the characteristics of evening cooling
441 mechanisms above urban green spaces considering dynamics of the urban boundary layer for
442 the three turbulence regimes. For each evening period (16-00 UTC), we analyse time series of
443 near-surface temperature, humidity, and wind measured in the built-up environment, urban
444 green infrastructures, and rural settings. To investigate the relative role of relevant cooling
445 mechanisms, i.e. radiative cooling of the surfaces, radiative cooling of the air through
446 radiative flux divergence, turbulent heat exchange, vertical mixing, and advection, it is helpful
447 to quantify conditions in the urban boundary layer. Therefore, in order to assess the relative
448 roles of surface-driven and atmospheric-driven processes, the conditions measured at the
449 surface are complemented by the analysis of the observations at the top of the Eiffel Tower
450 (287 m AGL), as well as vertical profiles of meteorological variables obtained from windsound
451 profile measurements.

452

453 4.1 Stagnant regime: strong park cooling effect combined with 454 strong UHI intensity

455

456 Here we focus on two nights that show the strongest park cooling effect intensity and most
 457 significant UHI intensity, classified as stagnant regime, i.e. 12-13/07 and 17-18/07. Both
 458 selected nights occur in high-pressure synoptic conditions with meso-scale subsidence over
 459 the region. Hot air advection driven by a secondary pressure low located west of the Iberian
 460 Peninsula led to 850 hPa temperatures near 20°C. Both nights are characterised by very warm
 461 conditions over the preceding daytime period with daily maximum air temperatures
 462 exceeding 32°C (see Fig.s 5a, 6a). Strong regional-scale UHI and park cooling intensities are
 463 due to sharp contrasts in peak cooling rates (Fig.s 5b and 6b) between built-up, park and rural
 464 settings that last for 4-6 hours. On both 12/07 and 17/07, an evening cooling (16-00 UTC) of -
 465 5°C, -9°C and -14°C is documented in the built-up, urban park and rural settings, respectively,
 466 as shown in Table 2.

467

	16-00 UTC cumulative temperature change [°C] (average cooling rate [°C/h])		
Regimes	Opera	Park	Rural
Stagnant Regime : Strong park cooling effect and strong UHI intensities	-5.1 (-0.6)	-9.1 (-1.1)	-14.0 (-1.8)
Intermediary Regime: Moderate park cooling effect and strong UHI intensities	-5.9 (-0.7)	-7.6 (-0.9)	-12.6 (-1.6)
Turbulent Regime: Weak park cooling effect and low UHI intensities	-9.6 (-1.2)	-9.4 (-1.2)	-13.1 (-1.6)

468 Table 2: 16-00 UTC cumulative evening temperature change and average cooling rate for the
 469 three types of turbulence regimes.

470

471 The relatively strong cooling rate in the urban park compared to the built-up settings suggests
472 that the surface-driven processes (i.e. radiative cooling and/or turbulent latent heat fluxes)
473 are rather efficient on those nights. In comparison, the air temperature at the top of the Eiffel
474 Tower peaks generally around 18 UTC, i.e. about 2 hr later than near the surface at values 2-
475 3°C colder than the near-surface air temperature (Fig.s 5a and 6a). After 18 UTC, the air starts
476 to cool with a rate of around -0.35°C/hr , which is nearly half the value of the near-surface
477 cooling rate measured in the built-up environment (Fig.s 5b and 6b). Hence, the air at 287 m
478 AGL is only moderately affected by the processes that cool the air close to the surface. This is
479 the first evidence of decoupling between the urban canopy layer (UCL) and the air above, and
480 the decrease in static instability in the urban boundary layer (UBL).

481

482 Further evidence of this decoupling due to static stability in the UBL can be found in the wind
483 speed measurements. Figures 5c and 6c show the time series of wind speed at 10 m AGL at
484 the Melun rural site, at 25 m AGL in the Montsouris urban park and at 287 m AGL at the Eiffel
485 Tower, for 12/07 and 17/07, respectively. A comparable temporal evolution of wind speed
486 can be observed in the evening hours on both days. During the afternoon, the wind speed at
487 both the urban park and the rural site are consistent (about $2\text{-}4\text{ m s}^{-1}$ and within $1\text{-}2\text{ m s}^{-1}$ of
488 each other). After about 18 UTC, the wind speed at 287 m AGL increases rapidly to reach 8-
489 10 m s^{-1} before 00 UTC, while the rural and urban park wind speed remains low at or below 2
490 m s^{-1} , i.e. often lower than during daytime. This is a second evidence that after sunset,
491 decoupling conditions occur between the surface layer and the air above.

492

493 Figures 5 and 6 g and h show vertical profiles of wind speed and direction derived from
494 windsound profiles launched at 16, 20 and 00 UTC over an urban park (PARK-E; Fig. 1) on 12/07
495 and a large urban wood (WOOD-B; Fig. 1) on 17/07, respectively. Both IOPs are characterised
496 by easterly winds with relatively little wind direction evolution in the evening. During daytime
497 (16 UTC), the wind speed is moderate ($2\text{-}4\text{ m s}^{-1}$) in the first 700 m of the atmospheric
498 boundary layer. The windsounds launched after sunset (near 20 UTC) reveal in both cases low
499 near-surface wind speed ($1.5\text{-}2.0\text{ m s}^{-1}$) that gradually increases with height (consistent with
500 results described in the previous paragraph). A 3 m s^{-1} wind shear can be observed on 17/07
501 between the surface and 200 m AGL. The wind shear is not as strong on 12/07, possibly

502 because the profile was measured 45 min earlier than on the other day. This wind shear is a
503 signature of the stabilisation of the atmosphere that inhibits the vertical transfer of
504 momentum and hence decouples the air aloft from surface drag effects, allowing the wind
505 speed to increase aloft (e.g. Barthelemie et al. 1996).

506

507 The windsonds launched at 00 UTC reveal even stronger windshear between surface and 200
508 m AGL, with maximum wind speed of around 6.5 m s^{-1} on both nights near 300 m AGL and a
509 decreasing wind speed above. This vertical structure is known as a low-level jet (LLJ), a
510 condition that occurs frequently on summer nights above Paris according to Céspedes et al.
511 (2024). Their work has shown that very low altitude LLJs are associated with low levels of
512 turbulence, due to the fact that they form in a statically stable atmosphere that inhibits
513 mechanically induced turbulence.

514

515 To characterise the importance of vertical mixing as a potential means for heat transfer
516 between the UCL and the nocturnal urban boundary layer, we use Doppler wind lidar
517 measurements to derive time series of vertical velocity variance (Figs 5d and 6d). During the
518 convective period of the two IOPs, the vertical velocity variance typically exceeds $0.5 \text{ m}^2 \text{ s}^{-2}$. It
519 then decreases rapidly around sunset. At 20 UTC, the values have dropped to less than 0.05
520 $\text{m}^2 \text{ s}^{-2}$ on both 12/07 and 17/07, and remain very low all night. This confirms the very low
521 vertical turbulent mixing in the UBL on both nights. It should be noted that in the stagnant
522 regime, the vertical velocity variance values are very low (less than $0.05 \text{ m}^2 \text{ s}^{-2}$) throughout
523 the LLJ layer that extends from 240 to about 500 m AGL or more (not shown). Hence even
524 though vertical velocity variance is not constant with height and the measurement height
525 (240 m AGL) is close the top of the UBL, we conclude that the vertical velocity variance value
526 at 240 m AGL is representative of the nocturnal urban boundary layer turbulence regime.

527

528 To characterise the role of vertical radiative flux divergence in the atmospheric boundary
529 layer, and to better understand the relative importance of surface-driven vs atmospheric-
530 driven processes, we analyse the vertical structure of temperature and its temporal evolution.
531 In the Eiffel Tower urban park (PARK-E), we find that near-surface temperatures measured by
532 the windsond on 12/07 are consistent with temperatures recorded by the Montsouris urban
533 park surface station (yellow circles in Fig. 5a). At 20 UTC, we observe a 1°C temperature

534 inversion between the surface and 50 m AGL (Fig. 5f). Above the inversion, the temperature
535 decreases adiabatically by about $-1^{\circ}\text{C}/100\text{ m}$ so that the potential temperature is nearly
536 constant in a statically neutral layer between 50 and 700 m (Fig. 5f). At 00 UTC, the surface-
537 based inversion has become stronger ($\Delta T_{\text{air}} = 2.5^{\circ}\text{C}$ and $\Delta \theta_{\text{air}} = 3.0^{\circ}\text{C}$ between the surface and
538 50 m AGL), and two elevated inversions have formed near 100 and 200 m AGL (Fig. 5f, g), with
539 $\Delta \theta_{\text{air}} = 0.5^{\circ}\text{C}$ followed by a statically stable layer with a $+0.2^{\circ}\text{C}/100\text{ m}$ lapse rate (Fig. 5g).

540

541 In the urban wood (WOOD-B), near-surface temperatures measured by the windsond on
542 17/07 are close to temperatures measured in the rural settings (green circles in Fig. 6a). With
543 3.5°C decrease over 50 m, the surface-based temperature inversion at 20 UTC (Fig. 6e) is
544 already stronger than the inversion observed at 00 UTC over PARK-E on 12/07. Above the
545 inversion, the temperature decreases adiabatically (Fig. 6e, f) and the potential temperature
546 profile confirms that the stable wood UBL is capped by a neutral layer above. At 00 UTC, the
547 surface-based inversion strengthens and extends aloft ($\Delta T_{\text{air}} = 5.0^{\circ}\text{C}/100\text{ m}$; $\Delta \theta_{\text{air}} = 6^{\circ}\text{C}/100$
548 m), followed by an elevated inversion near 250 m AGL (Fig. 6f, g). The potential temperature
549 profile is stable between 100 and 300 m AGL ($+1.0^{\circ}\text{C}/100\text{ m}$) and moderately stable
550 ($+0.2^{\circ}\text{C}/100\text{ m}$) above (Fig. 6g).

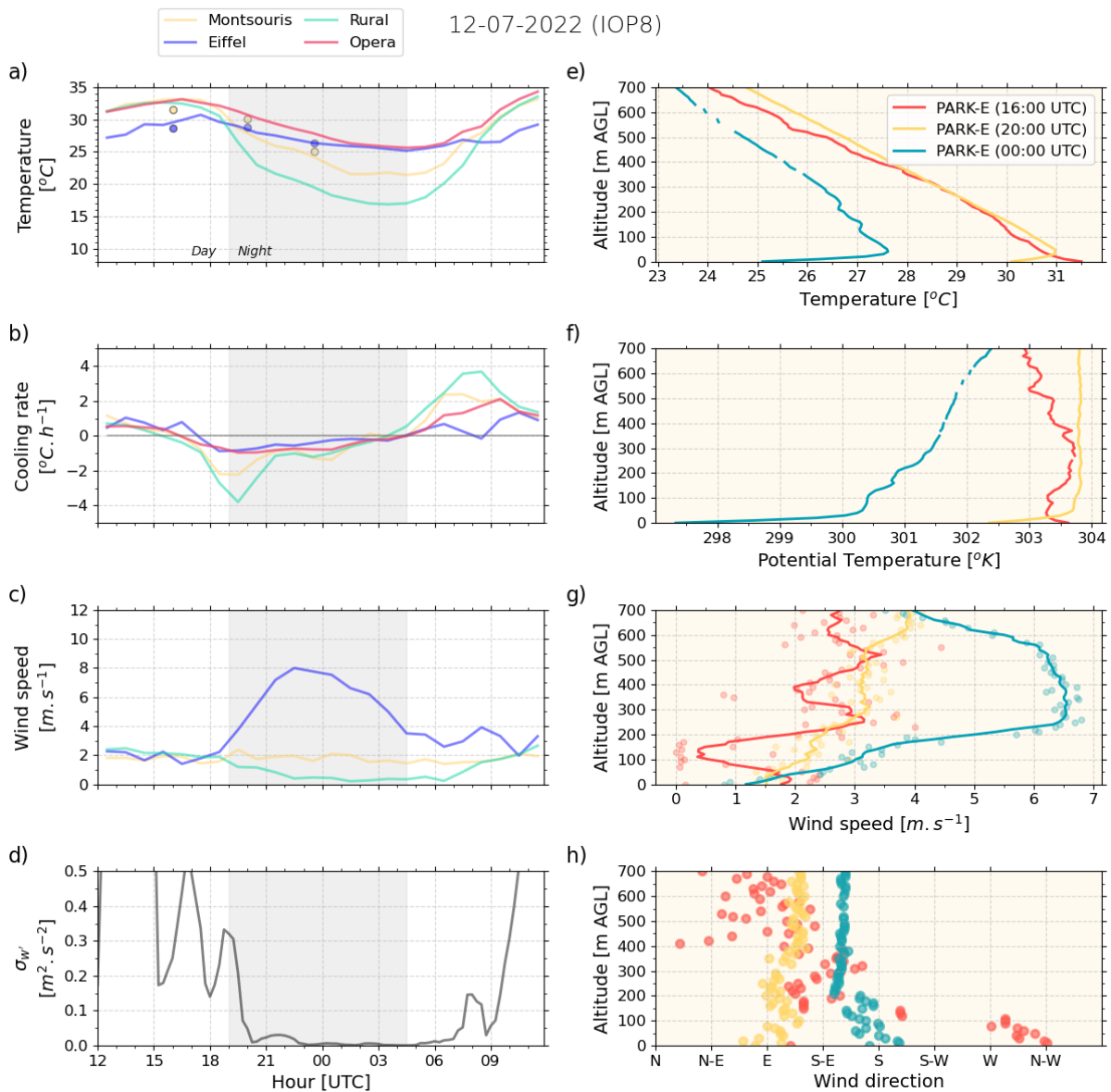
551

552 These elevated inversions observed both over the urban park and urban wood could be
553 formed through localised radiative cooling, subsidence and/or advection of statically stable
554 rural air that is commonly observed above nocturnal UBL (e.g. Tsiringakis et al. 2022). Elevated
555 inversions in nocturnal UBLs are simulated and studied extensively in Martilli (2002). The drag
556 and turbulent kinetic energy production induced by the urban structure increases with
557 increasing wind speed. Vertical mixing of potential temperature leads to a local minimum of
558 temperature at the location of maximum turbulence through a negative turbulent heat flux.
559 According to Martilli (2002), the net result of the vertical turbulent transport is to heat the
560 layer below the base of the inversion and to cool the inversion layer. Cooling of the inversion
561 layer (roughly between 200 and 300 m AGL) is clearly seen on the both windsond temperature
562 profiles measured at 00 UTC.

563

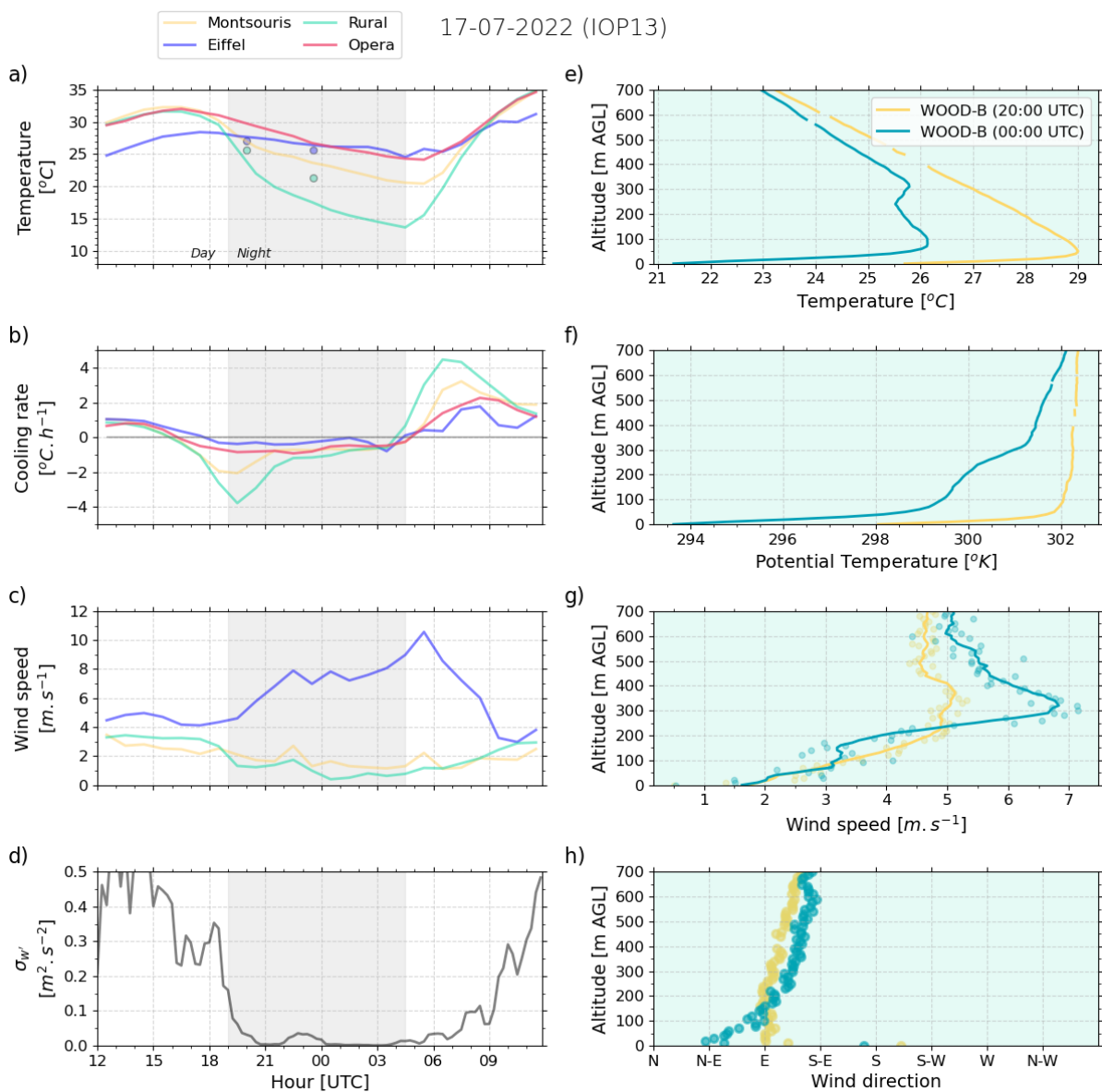
564 We can conclude that the conditions of stagnant regime, combining strong park cooling
565 effects and strong UHI intensities, are associated with a significant surface-based inversion

566 that leads to the decoupling not only of the rural nocturnal boundary layer from the residual
 567 layer but also between the urban boundary layer and the neutral layer above. The strong
 568 stratification suppresses nearly any turbulent vertical motion so that the UBL height is rather
 569 shallow - even below the top of the Eiffel Tower. As the flow is no longer subject to surface
 570 drag, a regional low-level jet forms that likely advects rural, statically stratified air over the
 571 UBL, which can influence the development of elevated inversions. The strong stratification in
 572 the park internal UBL is the result of cooling dominated by radiative flux divergence due to
 573 low turbulent mixing.
 574
 575



576

577 Figure 5: Time series and windsonde profile measurements for July 12, 2022. a-d) Time series
 578 measurements from 12 UTC to 12 UTC (D+1). a) Temperature at Montsouris Park, Rural
 579 settings, Opera (built-up) and top of Eiffel Tower. The coloured dots show the temperature
 580 measured by windsonds at 16, 20, and 00 UTC, respectively at park level and at the height of
 581 the Eiffel Tower (287m AGL). b) Cooling rate at Montsouris, Rural, Opera and Eiffel Tower. c)
 582 Wind speed at Montsouris, Rural, and Eiffel Tower. d) Vertical velocity variance from DWL at
 583 240 m AGL at QUALAIR-SU site. e-h) Vertical profiles from radiosonde measurements
 584 released in PARK-E at 16, 20, and 00 UTC, respectively. e) Temperature profile. f) Potential
 585 temperature profiles. g) Wind speed profiles. h) Wind direction profiles.



587
 588 Figure 6: same as Fig. 5 for July 17, 2022.

589
 590

591
592
593
594
595
596
597
598
599

600 4.2 Intermediary regime: moderate park cooling effect 601 combined with strong UHI intensity

602

603 The evening of 15-16/07, compared to those discussed in Section 4.1, is characterised by
604 weaker cooling between 16 and 00 UTC in the rural setting and urban park, and stronger
605 cooling in the built-up environment, as shown in Table 2. It is classified in the intermediary
606 regime. Cooling peaks near $-3^{\circ}\text{C}/\text{hr}$ in the rural setting and $-1.5^{\circ}\text{C}/\text{hr}$ in urban park, which is
607 slightly less than for the cases of Section 4.1 (Fig. 7b). For this regime, the nocturnal near-
608 surface wind only decreases in the rural setting while it increases in the urban park after 21
609 UTC as the wind aloft picks up (Fig. 7c) which indicates that vertical momentum transfer is
610 less inhibited above the urban surface. Figure 7d shows that the vertical turbulent mixing
611 remains above $0.1 \text{ m}^2 \text{ s}^{-2}$ after sunset and increases to $0.2 \text{ m}^2 \text{ s}^{-2}$ during the evening which
612 confirms that the UBL remains turbulent during the night.

613

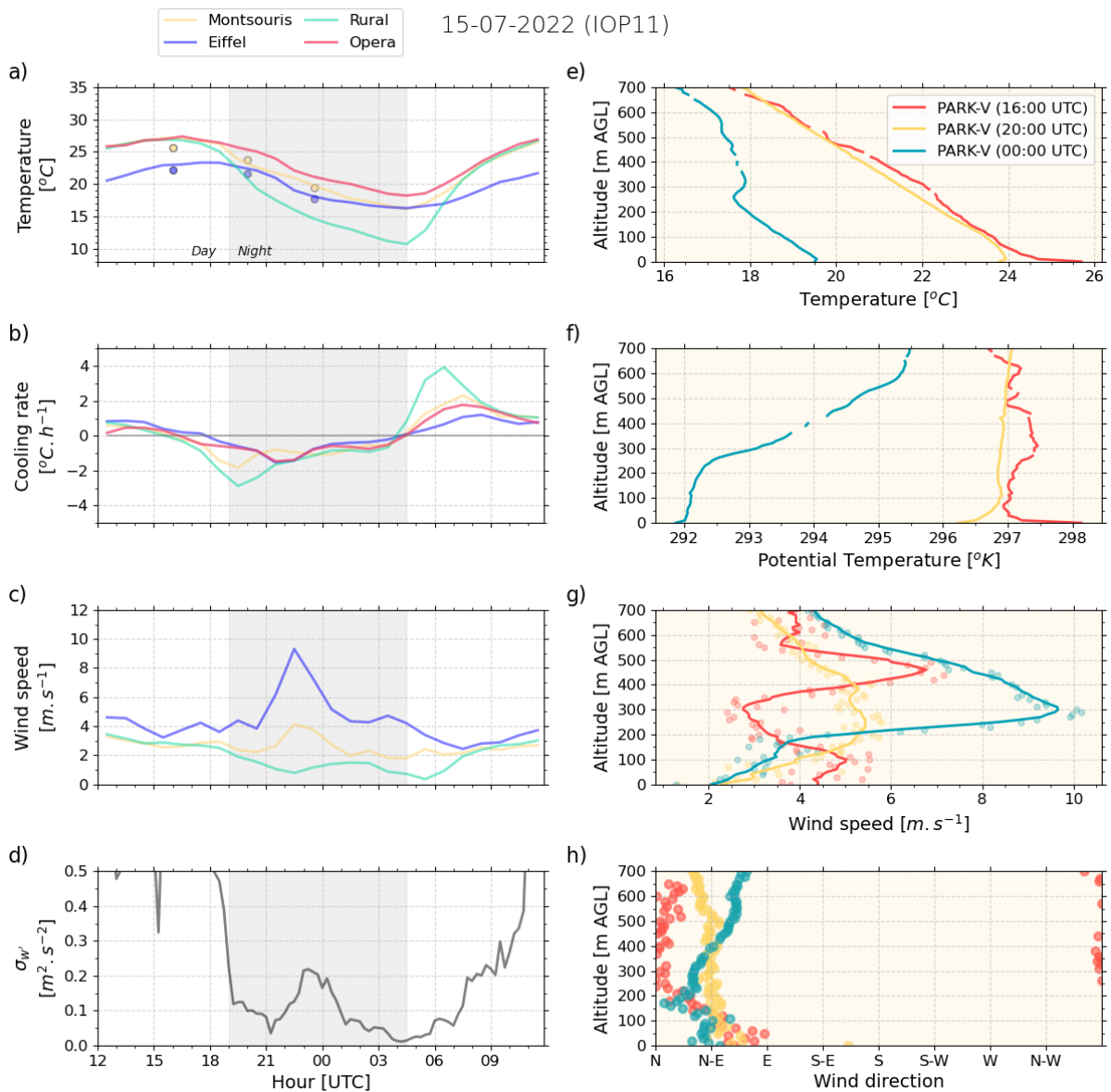
614 The windsound profiles carried out in the La Villette urban park (PARK-V on Fig. 1), for which
615 the vegetated area is comparable to that of the Montsouris urban park, reveal at 20 UTC a
616 slight surface-based inversion with a neutral layer above, while at 00 UTC under brisker
617 turbulent mixing the UBL remains near-neutral from the ground up to a temperature
618 inversion near 300 m AGL. It is then likely that the UBL remains neutral due to sensible heat
619 flux originating from the hot surface combined with turbulent mixing and from the
620 temperature inversion above. Again, a clear low-level jet with peak horizontal velocity $> 9 \text{ m}$

621 s^{-1} near the height of the temperature inversion suggests that stably stratified air from rural
 622 surroundings is advected over the city.

623

624 The intermediary regime highlights that while the rural nocturnal layer becomes statically
 625 stable during the evening, as evidenced by the very low near-surface wind speed at the rural
 626 site, the UBL remains statically neutral. Vertical turbulent mixing in the UBL prevents a
 627 temperature inversion to form in the UCL, even above the urban green space.

628



629

630 Figure 7: same as Fig. 5 for July 15, 2022 (IOP11)

631

632

633

634

635

636

637

638 4.3 Turbulent regime: weak park cooling effect combined with 639 weak regional UHI intensity

640

641 The evening of 04/07, classified in the turbulent regime, is characterised by nearly identical
642 cooling rates in built-up settings, urban green spaces, as well as aloft at the top of the Eiffel
643 Tower. Cooling peaks near -2 to -2.5°C/hr at all locations (Fig. 8b). Wind speed at both the
644 rural settings and the urban park does not decrease after sunset, but rather increases after
645 18 UTC as the wind aloft picks up (Fig. 8c). In addition to the strong advection effects, the UBL
646 remains turbulent during the night as turbulent vertical mixing remains above $0.2 \text{ m}^2\text{s}^{-2}$ after
647 sunset (Figure 8d), both indicating that vertical momentum transfer is not inhibited across the
648 region.

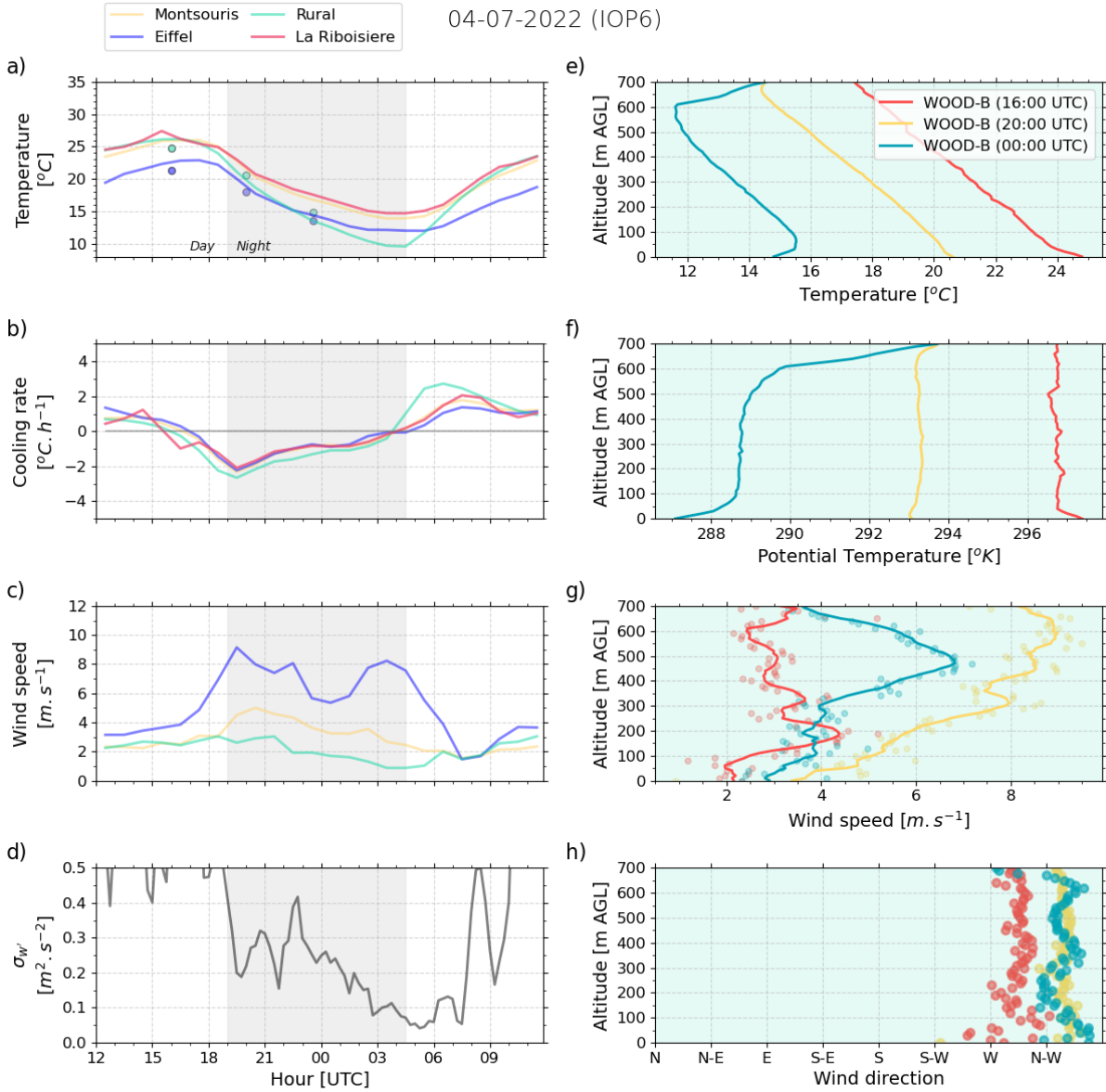
649

650 The windsound profiles carried out at the Bois de Boulogne large urban wood (WOOD-B in Fig.
651 1), detected a neutral UBL from 0 to 700 m AGL at 20 UTC. At 00 UTC, under continued brisk
652 turbulent mixing, a weak 1°C temperature inversion forms over the large green space while
653 the neutral UBL extends from 100m to 600 m AGL and is capped by a 5°C temperature
654 inversion.

655

656

657



658

659 Figure 8: same as Fig. 5 for July 04, 2022

660

661

662

663

664

665

666

667

668

669 5 - Characteristics and impacts of turbulence 670 regimes

671

672 To better understand the impact of wind, turbulence and static stability on differential cooling
673 between built-up areas, urban parks and rural settings, we analyse the characteristics of the
674 three turbulence regimes encountered during summer 2022. First, we study the diurnal
675 evolution of wind and turbulence in built-up settings, urban green spaces and rural
676 surroundings (Section 5.1) and then investigate the atmospheric static stability in the built-up
677 surfaces and green infrastructures (Section 5.2) for the three regimes. Finally, we analyse the
678 diurnal cycle of temperature and discuss the nocturnal cooling in built-up environments,
679 green infrastructures and rural settings for the three regimes (Section 5.3).

680 5.1 Wind and turbulent mixing characteristics of turbulence 681 regimes

682 First, we study how wind speed evolves at diurnal scales over the city (Montsouris urban
683 park), in the rural setting (Melun), and aloft (top of Eiffel Tower) for the turbulence regimes
684 identified in Section 3 (Fig. 9).

685

686 In the stagnant regime (highest UHI intensity and lowest vertical velocity variance), we find
687 that at sunset, when vertical mixing drops, the wind speed aloft increases while the near-
688 surface wind speed decreases both over the urban park and in the rural setting (Fig. 9a).
689 Vertical velocity variance reaches values below $0.05 \text{ m}^2 \text{ s}^{-2}$ shortly after sunset. Not only the
690 rural nocturnal boundary layer but also the UBL becomes stratified, thereby inhibiting vertical
691 transfer of momentum. The stable UBL becomes decoupled from the neutral layer above,
692 allowing near-surface wind speeds to decrease, on average below 2 m s^{-1} , through surface
693 drag, while wind speed aloft experiences reduced friction and hence increases.

694

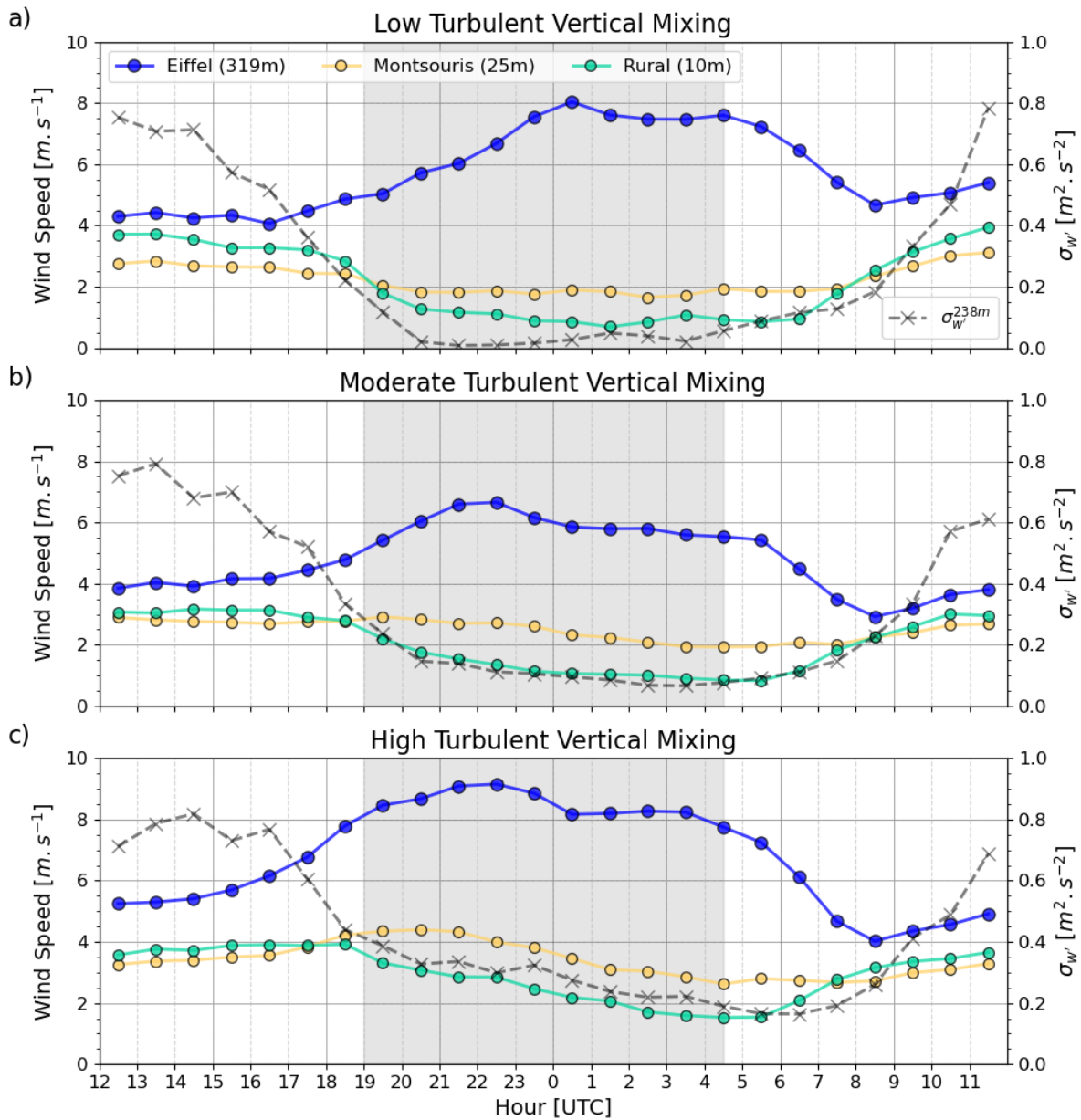
695 In the intermediate regime (strong ΔUHI and moderate vertical velocity variance), we observe
696 that on average, the vertical velocity variance decreases later than in the stagnant regime and
697 it is 50 % stronger at sunset, reaching $0.15 \text{ m}^2 \text{ s}^{-2}$ on average during the night (Fig. 9b). The

698 near-surface wind speed in the rural setting decreases at sunset similarly to the stagnant
699 regime, so we can hypothesise that the atmosphere becomes stable in the rural environment.
700 In the urban green spaces, the near-surface wind speed remains unchanged after sunset,
701 which is consistent with a continued vertical transfer of momentum. Still, the stable
702 stratification over the rural area tends to favour the formation of a low-level jet, a
703 phenomenon that occurs in Paris in 70% of the nights in summer 2022 (Cespedes et al. 2024),
704 so that the wind speed above the neutral UBL can double in magnitude between noon and
705 midnight.

706

707 In the turbulent regime (low UHI intensity and high vertical velocity variance) vertical velocity
708 variance in the UBL is on average above $0.3 \text{ m}^2 \text{ s}^{-2}$ at sunset (Fig. 9c). Near-surface wind speed
709 in the rural setting remains above 3 m s^{-1} on average, while central urban wind speeds
710 increase consistently across the UBL, i.e. both near the surface and at the top of the Eiffel
711 Tower.

712



713

714 Figure 9 : Average diurnal cycles over summer 2022 for each of the turbulence regimes
 715 (stagnant at the top, intermediary in the middle, and turbulent at the bottom): wind speed
 716 measured at Melun (rural site); Montsouris park (urban park); top of Eiffel Tower; and vertical
 717 velocity variance at 240 m AGL derived from Doppler Lidar measurements.

718 5.2 Atmospheric stability characteristics of turbulence regimes

719

720 In Section 4, we found evidence that the static stability above urban parks and urban woods
 721 can vary significantly depending on the turbulent vertical mixing in the UBL. To study this
 722 variability, we derive the potential temperature lapse rates for each windsound profile carried

723 out at 20 and 00 UTC above urban woods and parks, as well as radiosonde profiles launched
724 at the same time from the built-up area of Bercy (URBAN-B location on Fig. 1) along the Seine
725 river, and plot them against the vertical velocity variance estimated from the DWL
726 measurements at the same time (Fig. 10). The potential temperature lapse rate is derived for
727 two vertical intervals, 0-50 m AGL representing the height over which surface-based
728 inversions are typically observed (also called park/wood internal boundary layer), and 100-
729 200 m AGL representing the nocturnal UBL. Vertical velocity variances shown in Fig. 10 are
730 one-hour average values. The turbulence regime derived for each evening (19-02 UTC) is also
731 shown. Fig. 10b reveals that, when the vertical velocity variance drops below $0.05 \text{ m}^2 \text{ s}^{-2}$
732 (corresponding mostly to the stagnant regime) the near-surface potential temperature lapse
733 rate above urban parks (about 20 ha) ranges $4\text{-}6^\circ\text{C}/100 \text{ m}$ while those above the woods (about
734 900 ha) can reach $8\text{-}14^\circ\text{C}/100 \text{ m}$. In the lowest vertical velocity variance conditions (< 0.025
735 $\text{m}^2 \text{ s}^{-2}$), near-surface potential temperature lapse rates in built-up areas also become positive
736 ranging $1\text{-}3^\circ\text{C}/100 \text{ m}$. This confirms that stable stratification can occur in all settings, but the
737 strength of the stratification depends on the surface type.

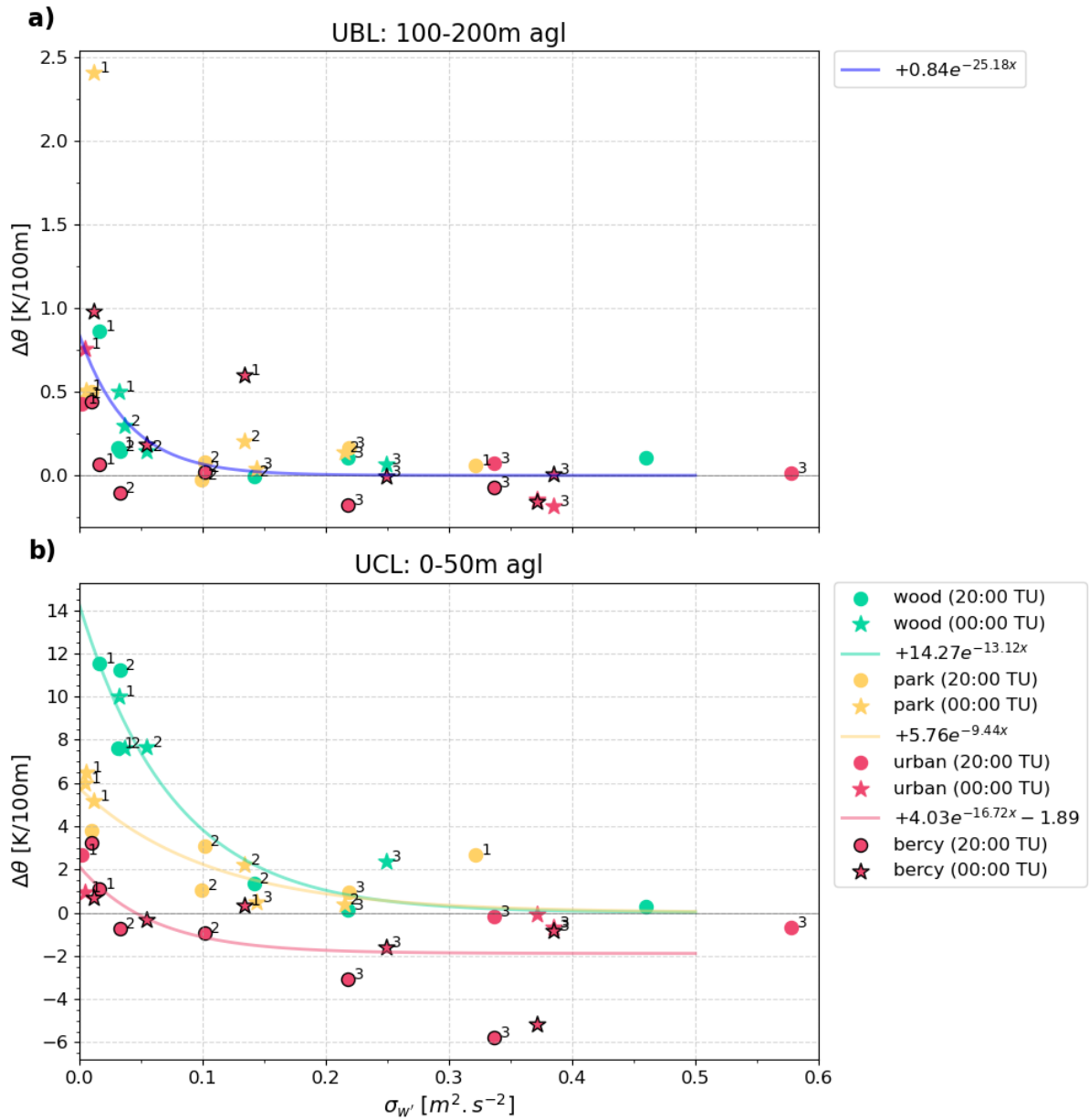
738 For vertical velocity variances ranging $0.1\text{-}0.2 \text{ m}^2 \text{ s}^{-2}$, near-surface potential temperature lapse
739 rates above parks and woods range between $0\text{-}3^\circ\text{C}/100 \text{ m}$, decreasing to near adiabatic
740 conditions ($0^\circ\text{C}/100 \text{ m}$) as turbulent mixing increases. In built-up areas, we find that near-
741 surface potential temperature lapse rates become negative (near $-1^\circ\text{C}/100 \text{ m}$) as soon as the
742 vertical velocity variance exceeds $0.05 \text{ m}^2 \text{ s}^{-2}$, a signature of a typical unstable urban surface
743 layer.

744 This analysis provides quantitative evidence that evening and night-time air temperature
745 conditions in the UCL become spatially heterogeneous when turbulent mixing in the UBL is
746 very weak. Only then it is possible for a strong temperature inversion to form over the urban
747 green space through the support of radiative flux divergence. The cool air remains in a local,
748 internal park/wood thermal boundary layer and does not mix with the relatively warm air in
749 the surrounding neighbourhoods. The significance and vertical extent of this cool air pool
750 increases with green space size, and it can be speculated that also green fraction and soil
751 moisture levels would enhance the effect.

752

753 The turbulent mixing in the UBL varies with the static stability of the UBL. As shown in Fig.
754 10a, when the potential temperature lapse rate at 100-200 m AGL increases to values near

755 +0.5°C/100m for all settings, including built-up areas, the vertical velocity variance decreases
 756 below 0.05 m² s⁻². No clear contrast in stability is found above the different surfaces,
 757 confirming that under the stagnant regime, the nighttime UBL is very shallow.
 758



759

760 Figure 10: Nighttime (20 and 00 UTC) potential temperature lapse rate above wood (green),
761 park (orange) and built-up areas (red) as a function of σ_w in the UBL (at 240 m AGL) for (a) a
762 layer between 100-200 m AGL and (b) a layer between 0-50 m AGL. Symbols indicate time
763 UTC. Urban labels with black borders correspond to data from radiosoundings launched from
764 the URBAN-B site and the others to data from windsounds (various sites). The number shows
765 the mean evening (19-02 UTC) turbulence regime for each case.

766

767 5.3 Impact of turbulence regimes on diurnal temperature 768 evolution

769

770 Ultimately, we want to determine how the turbulence regimes can impact the nocturnal
771 cooling provided by urban green infrastructures. Figure 11 shows the mean diurnal cycles of
772 temperature for stagnant, intermediary and turbulent regimes (a, b, and c, respectively). The
773 temperature diurnal cycles are normalised by subtracting the temperature measured at 16
774 UTC (peak daytime temperature). On average, daytime peak temperatures are highest for the
775 stagnant regime near 31°C, while they peak at about 27°C for the other two regimes. Figure
776 11 shows that after 16 UTC, the temperature at all sites decreases to a minimal value by the
777 next morning at sunrise. In 12 hours, the temperatures drop between 8 and more than 14°C
778 depending on the surface type and the turbulence regime. The stagnant regime reveals the
779 strongest contrasts between the settings (Fig. 11a). At 00 UTC, five hours after sunset, the
780 built-up neighbourhood cooled by 5.5°C, while the urban park cooled by 9.0°C and the rural
781 sites by almost 13.8°C. This confirms earlier findings (Table 2 and Section 5.2) that under low
782 turbulent vertical mixing, the radiative cooling of the surface in urban park and rural settings
783 combined with low turbulent vertical mixing provides an efficient cooling of the near-surface
784 atmosphere. In such conditions, urban parks can provide significantly cooler conditions than
785 the built-up neighbourhoods nearby.

786 In the intermediary regime, the evening cooling rate in the built-up environment is slightly
787 larger than for the stagnant regime (-6.2°C at 00 UTC, Fig. 11b). In the urban park, the
788 increased UBL turbulent vertical mixing reduces the strength of the near-surface radiative flux
789 divergence. The evening cooling in the urban park is not as strong (-7.5°C at 00 UTC) as in the

790 stagnant regime. In the rural setting, the evening cooling is also reduced in the intermediary
791 regime (-11.7°C at 00 UTC) compared to the stagnant regime, revealing that turbulence is also
792 likely stronger in the rural nocturnal boundary layer.

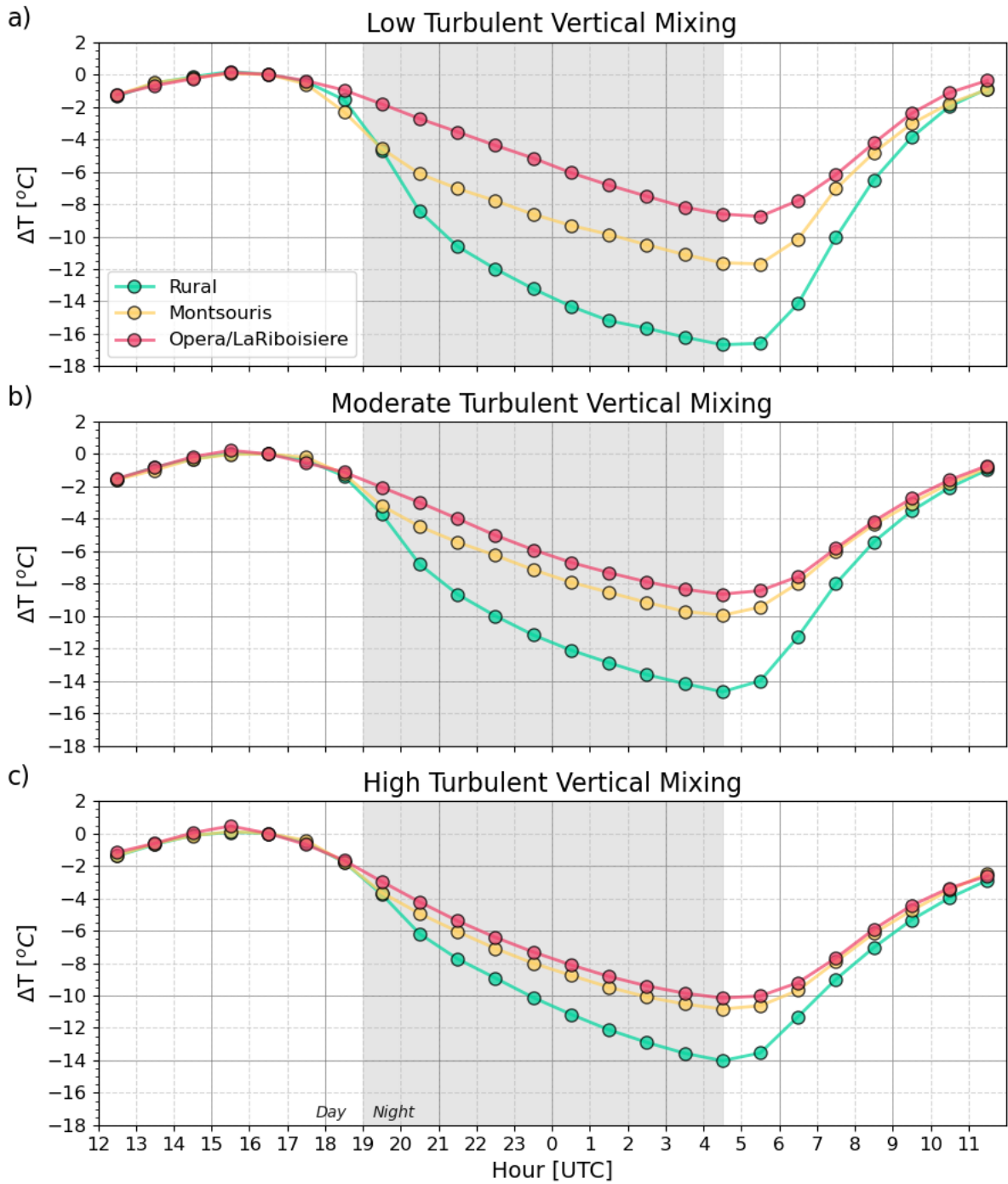
793 In the turbulent regime, with stronger turbulent vertical mixing and higher near-surface wind
794 speed than in the other regimes, the efficiency of the surface-driven cooling in the rural
795 setting is even more reduced, which limits the cooling compared to less turbulent conditions
796 (-10.6°C at 00 UTC, Fig. 11c). In the built-up environment, the air temperature drops by 7.6°C
797 between 16 and 00 UTC, i.e. 1.5-2°C more than in the other regimes. In this turbulent regime,
798 the city centre benefits from the cooling of the rural surroundings through advection – the
799 cooler air is mixed down into the UBL. In the urban park, two competing processes occur. The
800 radiative flux divergence is reduced by the strong mixing, but this again means cooler air
801 advected from rural surroundings is efficiently mixed down thereby contributing to a strong
802 cooling also in the urban park. Hence, we find that the temperature drops by 8.3°C on average
803 between 16 and 00 UTC, which is in between the stagnant and intermediary regime cooling.

804

805

806

807



808

809 Figure 11: diurnal cycle of temperature difference relative to the temperature at 16 UTC at
 810 Melun (rural site), Montsouris park (urban park) and Opera/Lariboisiere (Built-up setting) for
 811 stagnant, intermediary and turbulent regimes.

812

813

814 6) Conclusions

815 This study shows that the nocturnal cooling effect of urban parks depends on their
816 characteristics, such as their size, but also on UBL turbulent mixing and static stability regimes
817 that drive the relative importance of radiative and mixing transport cooling processes in the
818 UCL. We find that turbulent vertical mixing conditions measured by a Doppler Lidar at about
819 240 m AGL in the city centre are a very useful indicator to distinguish different evening cooling
820 regimes in the urban environment. These findings are summarised on a schematic (Fig. 12)
821 that represents, for each turbulent mixing regime, typical night-time vertical profiles of wind
822 and potential temperature above the urban environment and key processes that affect
823 nocturnal cooling.

824

825 Highest green space nocturnal cooling intensity occurs under stable stratification in the UBL
826 (statically stable, low turbulent mixing: vertical velocity variance of less than $0.05 \text{ m}^2 \text{ s}^{-2}$) over
827 both rural settings and urban parks. This stagnant regime is associated with large-scale
828 subsidence and large-scale advection of warm air aloft. The potential temperature profiles
829 above the urban parks and woods become statically stable soon after sunset due to radiative
830 cooling of the surface and subsequent cooling of the air by radiative flux divergence, in the
831 absence of a significant turbulent heat flux. A few hours after sunset, the entire UBL becomes
832 on average statically stable (about 200-250 m deep) due to subsidence and advection of the
833 stable rural air above the urban environment. Even if the heat release from the urban surface
834 would in theory lead to an unstable/near neutral urban boundary layer at night, we observe
835 that the strong stabilisation from above limits it strongly in height, or even totally inhibits it.
836 At the top of the UBL, a low-level jet develops over the night with peak wind speed, but
837 mechanical turbulence is inhibited by the static stability of the UBL. The advected rural air
838 mass remains stable above the urban environment because of unusually low vertical mixing
839 conditions. This stagnant regime exhibits the strongest evening cooling in both rural settings
840 and urban parks, and the weakest cooling in the built-up environment, hence strong nocturnal
841 temperature contrasts occur in the city depending on the vegetation fraction. In this regime,
842 the cooling effect of green infrastructure will depend on their size and likely on the vegetation
843 fraction of these areas. In this stagnant regime, we find comparable nocturnal cooling rates
844 (peaking at -2°C/hr around sunset) and static stability in the UCL (lapse rate near $6^\circ\text{C}/100\text{m}$

845 at 00 UTC) above the Montsouris park (15 ha) and the Eiffel tower park (24 ha) that are
846 roughly of the same size. Above urban woods (about 900 ha) near-surface lapse rates can
847 reach twice the value observed above urban parks (near 12°C/100m at 00 UTC). This leads to
848 the development of an internal UBL, about 50 m (100 m) deep, above urban parks (woods).

849

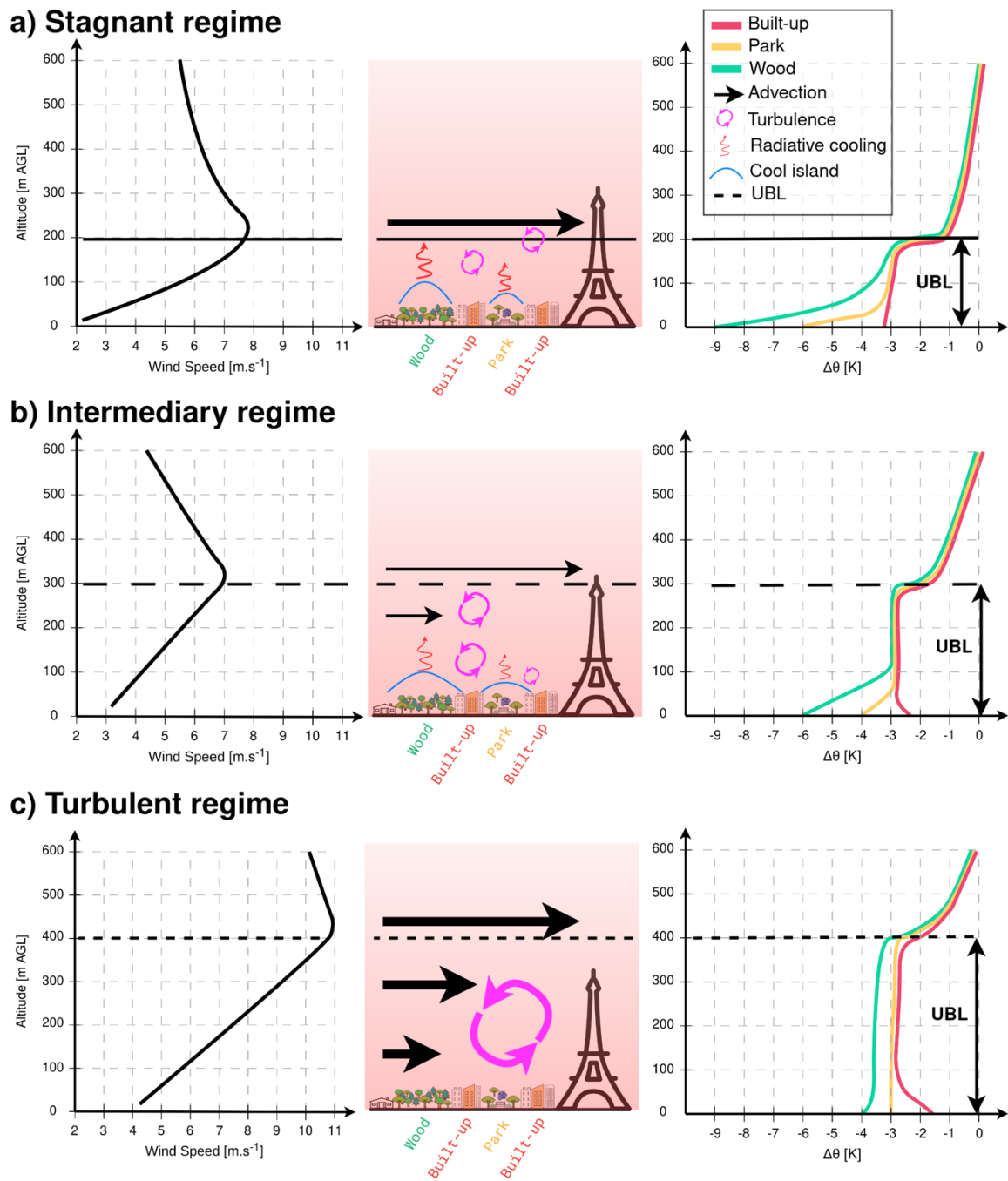
850 A second regime is identified, characterised by moderate turbulent vertical mixing in the UBL
851 (for vertical velocity variance between 0.1 and 0.2 m² s⁻²). Under this intermediary regime, the
852 potential temperature profiles above the urban park become neutral after sunset. A small
853 temperature inversion (<1°C above urban parks, <3°C above urban woods) can be found in
854 the UCL. A few hours after sunset, the UBL remains statically neutral up to 250-300 m due to
855 positive turbulent heat flux at the surface and at the top of the UBL which is characterised by
856 a temperature inversion. Advection of rural air brings a statically stable layer above the UBL.
857 Under this intermediary regime, the evening cooling in rural settings is about 2°C less than in
858 the stagnant regime. Two hours after sunset, the cooling in the urban park is also 2°C less
859 than in the stagnant regime, while the built-up environment is slightly cooler than in the
860 stagnant regime. There is probably vertical and also horizontal air mixing (advection or local
861 turbulence), which diminishes the cooling effect of small to medium-sized parks (15-25ha) by
862 mixing air from surrounding dense neighbourhoods. Hence, in the intermediary regime the
863 intra-urban temperature contrasts between areas with varying vegetation fractions are
864 significantly reduced.

865

866 The third regime identified in this study results in the weakest nocturnal temperature
867 contrasts. Compared to the stagnant and intermediary regimes, the turbulent regime is
868 characterised by stronger advection and mesoscale circulation, wind shear and turbulent
869 vertical mixing. The UBL above the urban park becomes neutral after sunset, with a depth
870 that is significantly increased (>400 m) compared to the two other regimes. The UBL remains
871 neutral even several hours after sunset. In this turbulent regime, the evening cooling rates
872 are nearly identical in the built-up environment and in the urban parks. In this regime, high
873 turbulence and wind mix the air and homogenise temperatures at a larger scale (district-to-
874 city scale) than in the intermediary regime (neighbourhood scale), completely encompassing
875 and erasing the cooling effect of parks.

876

877 As statically stable low turbulent mixing conditions occur during the strongest heat waves due
878 to large-scale subsidence and advection of hot air, it is important to maintain spatially
879 distributed and accessible vegetated cool island spots in the city so that people can benefit
880 from cooler outdoor night-time conditions after being exposed to significant daytime heat
881 stress.
882



884

885 Figure 12. Typical night-time (near 00 UTC) vertical structure of wind speed (left) and
 886 potential temperature (right) in the urban boundary layer, observed during a)
 887 stagnant, b) intermediate, and c) turbulent mixing regimes. Potential temperature
 888 profiles are represented above built-up environments (red), urban parks (yellow) and
 889 urban woods (green). Key processes (advection, turbulent mixing, radiative cooling)
 890 affecting nocturnal cooling in the UBL are represented (centre).

891 Data availability

892 All raw data are available from the AERIS data centre catalogue at <https://paname.aeris->
893 [data.fr/data-catalogue-2/](https://paname.aeris-data.fr/data-catalogue-2/).

894

895 Author contributions

896 MH, SK, AL, and VM planned the campaign; MH, SK, JFR, JCD and JC performed the
897 measurements; MH, JFR, SK and JC analysed the data; MH and SK wrote the manuscript draft;
898 JFR produced the figures; AL, VM and TN reviewed and edited the manuscript.

899

900 Competing interests

901 The authors declare that they have no conflict of interest.

902

903 Acknowledgements

904

905 The PANAME experimental program benefited from several supports, including the research
906 project H2C funded by the French national agency for research (ANR) with the reference ANR-
907 20-CE22-0013, the Research Demonstration Project for Paris Olympics 2024 funded by
908 Météo-France and the Weather Meteorological Organization, the Paris Region PhD program
909 2020, investments from DIM QI2, OBS4CLIM-PIA3, CNRS-INSU and the ACTRIS research
910 infrastructure, and data management (AERIS national data and services center). The authors
911 would like to thank all the volunteers and participants who contributed to the success of the
912 SOP 2022, in particular the teams and many volunteers who carried out the windsonde
913 releases in the parks in the evening and at night and the radiosoundings at Bercy. Thanks are
914 extended to Hugo Ricketts for training the IPSL team to operate windsonds, with the support
915 of the European COST action PROBE. Authors would like to express their thanks to the
916 QUALAIR-SU scientific team who enabled the Doppler Lidar deployment on the site at

917 Sorbonne Université.

918

919 References

920 Aram, F., Higuera García, E., Solgi, E., and Mansournia S.: Urban green space cooling effect
921 in cities, *Heliyon*, 5, <https://doi.org/10.1016/j.heliyon.2019.e01339>, 2019.

922

923 Barradas, V. L.: Air temperature and humidity and human comfort index of some city parks
924 of Mexico City, *Int. J. Biometeorol.*, 35, 24–28, <https://doi.org/10.1007/BF01040959>, 1991.

925

926 Basu, R. and Samet, J. M.: Relation between Elevated Ambient Temperature and Mortality:
927 A Review of the Epidemiologic Evidence, *Epidemiologic Reviews*, Volume 24, Issue 2, Pages
928 190–202, <https://doi.org/10.1093/epirev/mxf007>, 2002.

929

930 Barthelmie, R. J., Grisogono, B., and Pryor, S. C.: Observations and simulations of diurnal cycles
931 of near-surface wind speeds over land and sea. *Journal of Geophysical Research:*
932 *Atmospheres*, 101(D16), 21327-21337, <https://doi.org/10.1029/96JD01520>, 1996.

933

934 Dahech, S., Charfi, S., and Madelin, M.: Représentativité des températures mesurées dans la
935 station météorologique Paris-Montsouris. *Climatologie*, 17, 5.
936 <https://doi.org/10.1051/climat/202017005>, 2020.

937

938 Bowler D. E., Buyung-Ali, L., Knight, T. M., and Pullin, A. S.: Urban greening to cool towns and
939 cities: A systematic review of the empirical evidence, *Landscape and Urban Planning*, Volume
940 97, Issue 3, Pages 147-155, ISSN 0169-2046,
941 <https://doi.org/10.1016/j.landurbplan.2010.05.006>, 2010.

942

943 Cai, X., Yang, J., Zhang, Y., Xiao, X., and Xia, J.: Cooling island effect in urban parks from the
944 perspective of internal park landscape, *Humanities and Social Sciences Communications*, 10,
945 674, <https://doi.org/10.1057/s41599-023-02209-5>, 2023.

946

947 Chang, C. C., Li, M-H., and Chang, S-D.: A preliminary study on the local cool-island intensity
948 of Taipei city parks, *Landscape and Urban Planning*, Volume 80, Issue 4, Pages 386-395, ISSN
949 0169-2046, <https://doi.org/10.1016/j.landurbplan.2006.09.005> , 2007.

950

951 Céspedes, J., Kotthaus, S., Preissler, J., Toupoint, C., Thobois, L., Drouin, M.-A., Dupont, J.-C.,
952 Fauchoux, A., and Haeffelin, M.: The Paris low-level jet during PANAME 2022 and its impact
953 on the summertime urban heat island, *Atmos. Chem. Phys.*, 24, 11477–11496,
954 <https://doi.org/10.5194/acp-24-11477-2024>, 2024.

955

956 Doick K. J., Peace, A., and Hutchings, T. R.: The role of one large greenspace in mitigating
957 London's nocturnal urban heat island, *Science of The Total Environment*, Volume 493, Pages
958 662-671, ISSN 0048-9697, <https://doi.org/10.1016/j.scitotenv.2014.06.048> , 2014.

959

960 Forceville G., Lemonsu, A., Gorla, S., Stempfelet, M., Host, S., Alessandrini, J-M., Cordeau, E.,
961 and Pascal, M.: Spatial contrasts and temporal changes in fine-scale heat exposure and
962 vulnerability in the Paris region, *Science of The Total Environment*, Volume 906, 167476, ISSN
963 0048-9697, <https://doi.org/10.1016/j.scitotenv.2023.167476> , 2024.

964

965 Gao, Z., Zaitchik, B. F., Hou, Y., and Chen, W.: Toward park design optimization to mitigate the
966 urban heat Island: Assessment of the cooling effect in five US cities, *Sustainable Cities and*
967 *Society*, 81, 103870. <https://doi.org/10.1016/j.scs.2022.103870>, 2022.

968

969 Grimmond, C. S. B., and Oke, T. R.: Turbulent Heat Fluxes in Urban Areas: Observations and a
970 Local-Scale Urban Meteorological Parameterization Scheme (LUMPS), *J. Appl. Meteor.*
971 *Climatol.*, 41, 792–810, [https://doi.org/10.1175/1520-](https://doi.org/10.1175/1520-0450(2002)041<0792:THFIUA>2.0.CO;2)
972 [0450\(2002\)041<0792:THFIUA>2.0.CO;2](https://doi.org/10.1175/1520-0450(2002)041<0792:THFIUA>2.0.CO;2) , 2002.

973

974 Haeffelin, M., Barthès, L., Bock, O., Boitel, C., Bony, S., Bouniol, D., Chepfer, H., Chiriaco, M.,
975 Cuesta, J., Delanoë, J., Drobinski, P., Dufresne, J-L., Flamant, C., Grall, M., Hodzic, A., Hourdin,
976 F., Lapouge, F., Lemaître, Y., Mathieu, A., Morille, Y., Naud, C., Noël, V., O'Hirok, W., Pelon, J.,
977 Pietras, C., Protat, A., Romand, B., Scialom, G., and Vautard, R.: SIRTA, a ground-based
978 atmospheric observatory for cloud and aerosol research. *Ann Geophys* 23:253–275,

979 <https://doi.org/10.5194/angeo-23-253-2005>, 2005.

980

981 Holmer, B., Thorsson, S., and Lindén, J.: Evening evapotranspirative cooling in relation to
982 vegetation and urban geometry in the city of Ouagadougou, Burkina Faso, International
983 Journal of Climatology, 33(15), 3089-3105 , <https://doi.org/10.1002/joc.3561>. , 2013.

984

985 Ibsen, P. C., Borowy, D., Dell, T., Greydanus, H., Gupta, N., Hondula, D. M., ... and Jenerette,
986 G. D.: Greater aridity increases the magnitude of urban nighttime vegetation-derived air
987 cooling, Environmental Research Letters, 16(3), 034011, DOI 10.1088/1748-9326/abdf8a ,
988 2021.

989

990 Keatinge, W. R., Donaldson, G. C., Cordioli, E., Martinelli, M., Kunst, A. E.: Mackenbach J P et
991 al. Heat related mortality in warm and cold regions of Europe: observational study, BMJ, 321
992 :670, <https://doi.org/10.1136/bmj.321.7262.670>, 2000.

993

994 Laj, P., Lund Myhre, C., Riffault, V., Amiridis, V., Fuchs, H., Eleftheriadis, K., ... and Vana, M.:
995 Aerosol, Clouds and Trace Gases Research Infrastructure–ACTRIS, the European research
996 infrastructure supporting atmospheric science, Bulletin of the American Meteorological
997 Society. <https://doi.org/10.1175/BAMS-D-23-0064.1>, 2024.

998

999 Lemonsu, A., Belair, S. and Mailhot, J.: The New Canadian Urban Modelling System: Evaluation
1000 for Two Cases from the Joint Urban 2003 Oklahoma City Experiment, Boundary-Layer
1001 Meteorol., 133, 47–70, <https://doi.org/10.1007/s10546-009-9414-2> , 2009.

1002

1003 Lemonsu, A., Vignié, V., Daniel, M., and Masson, V.: Vulnerability to heat waves: Impact of
1004 urban expansion scenarios on urban heat island and heat stress in Paris (France), Urban
1005 Climate, Volume 14, Part 4, Pages 586-605, ISSN 2212-0955,
1006 <https://doi.org/10.1016/j.uclim.2015.10.007>, 2015.

1007

1008 Lemonsu, A., Alessandrini, J.M., Capo, J., Claeys, M., Cordeau, E., de Munck, C., Dahech, S.,
1009 Dupont, J.C., Dugay, F., Dupuis, V., Forceville, G., Garrigou, S., Garrouste, O., Goret, M., Gorla,
1010 S., Haeffelin, M., Host, S., Joly, C., Keravec, P., Kotthaus, S., Laruelle, N., Madelin, M., Masson,

1011 V., Mauclair, C., Nagel, T., Pascal, M., Ribaud, J-F., Roberts, G., Rosso, A., Roy, A., Sabre, M.,
1012 Sanchez, O., Stempfelet, M., Wei, W., Wilson, R., and Wurtz, J.: The heat and health in cities
1013 (H2C) project to support the prevention of extreme heat in cities, Climate Services, 100472,
1014 ISSN 2405-8807, <https://doi.org/10.1016/j.cliser.2024.100472> , 2024.
1015
1016 Lin, Y., Wang, C., Yan, J., Li, J., and He, S. : Observation and Simulation of Low-Level Jet Impacts
1017 on 3D Urban Heat Islands in Beijing: A Case Study, *J. Atmos. Sci.*, 79, 2059–2073,
1018 <https://doi.org/10.1175/JAS-D-21-0245.1>, 2022.
1019
1020 Martilli, A.: Numerical Study of Urban Impact on Boundary Layer Structure: Sensitivity to Wind
1021 Speed, Urban Morphology, and Rural Soil Moisture. *J. Appl. Meteor. Climatol.*, 41, 1247–1266,
1022 [https://doi.org/10.1175/1520-0450\(2002\)041<1247:NSOUIO>2.0.CO;2](https://doi.org/10.1175/1520-0450(2002)041<1247:NSOUIO>2.0.CO;2) . , 2002.
1023
1024 Morris, C. J. G., Simmonds, I., and Plummer, N.: Quantification of the Influences of Wind and
1025 Cloud on the Nocturnal Urban Heat Island of a Large City, *J. Appl. Meteor. Climatol.*, 40, 169–
1026 182, [https://doi.org/10.1175/1520-0450\(2001\)040<0169:QOTIOW>2.0.CO;2](https://doi.org/10.1175/1520-0450(2001)040<0169:QOTIOW>2.0.CO;2) . , 2001.
1027
1028 Murage, P., Hajat, S., and Kovats, R. S.: Effect of night-time temperatures on cause and age-
1029 specific mortality in London, *Environmental Epidemiology* 1(2):p e005, DOI:
1030 10.1097/EE9.0000000000000005, 2017.
1031
1032 Oke, T. R.: The distinction between canopy and boundary-layer urban heat islands,
1033 *Atmosphere*, 14(4), 268–277. <https://doi.org/10.1080/00046973.1976.9648422> , 1976.
1034
1035 Oke, T.R.: The energetic basis of the urban heat island, *Q.J.R. Meteorol. Soc.*, 108: 1-24,
1036 <https://doi.org/10.1002/qj.49710845502> , 1982.
1037
1038 Oke, T. Towards better scientific communication in urban climate, *Theor. Appl. Climatol.* 84,
1039 179–190, <https://doi.org/10.1007/s00704-005-0153-0> , 2006.
1040
1041 Oke, T. R., Mills, G., Christen, A., and Voogt, J. A.: *Urban climates*, Cambridge University Press,
1042 <https://doi.org/10.1017/9781139016476> , 2017.

1043
1044
1045
1046
1047
1048
1049
1050
1051
1052
1053
1054
1055
1056
1057
1058
1059
1060
1061
1062
1063
1064
1065
1066
1067
1068
1069
1070
1071
1072
1073
1074

Pirard, P., Vandentorren, S., Pascal, M., Laaidi, K., Le Tertre, A., Cassadou, S., and Ledrans M.: Summary of the mortality impact assessment of the 2003 heat wave in France, *Euro Surveill.*;10(7):pii=554. <https://doi.org/10.2807/esm.10.07.00554-en> , 2005.

von Rohden, C., Sommer, M., Naebert, T., Motuz, V., and Dirksen, R. J.: Laboratory characterisation of the radiation temperature error of radiosondes and its application to the GRUAN data processing for the Vaisala RS41, *Atmos. Meas. Tech.*, 15, 383–405, <https://doi.org/10.5194/amt-15-383-2022>, 2022.

Royé, D., Sera, F., Tobías, A., Lowe, R., Gasparrini, A., Pascal, M., de’Donato, F., Nunes, B., and Teixeira, J. P.: Effects of Hot Nights on Mortality in Southern Europe. *Epidemiology* 32(4):p 487-498, | DOI: 10.1097/EDE.0000000000001359 , 2021.

Shashua-Bar, L., and Hoffman, M. E.: Vegetation as a climatic component in the design of an urban street: An empirical model for predicting the cooling effect of urban green areas with trees, *Energy and Buildings*, Volume 31, Issue 3, Pages 221-235, ISSN 0378-7788, [https://doi.org/10.1016/S0378-7788\(99\)00018-3](https://doi.org/10.1016/S0378-7788(99)00018-3) , 2000.

Steenefeld, G. J., van de Wiel, B. J. H. , and Holtslag, A. A. M.: Modeling the Evolution of the Atmospheric Boundary Layer Coupled to the Land Surface for Three Contrasting Nights in CASES-99, *J. Atmos. Sci.*, 63, 920–935, <https://doi.org/10.1175/JAS3654.1> , 2006.

Steenefeld, G. J., Wokke, M. J. J. , Groot Zwaafink, C. D., Pijlman, S., Heusinkveld, B. G. Jacobs, A. F. G., and Holtslag, A. A. M.: Observations of the radiation divergence in the surface layer and its implication for its parameterization in numerical weather prediction models, *J. Geophys. Res.*, 115, D06107, doi:[10.1029/2009JD013074](https://doi.org/10.1029/2009JD013074), 2010.

Taha, H., Akbari, H. and Rosenfeld, A.: Heat island and oasis effects of vegetative canopies: Micro-meteorological field-measurements. *Theor Appl Climatol* 44, 123–138, <https://doi.org/10.1007/BF00867999> , 1991.

1075 Tsiringakis, A., Theeuwes, N.E., Barlow, J.F. *et al.* Interactions Between the Nocturnal Low-
1076 Level Jets and the Urban Boundary Layer: A Case Study over London. *Boundary-Layer*
1077 *Meteorol* **183**, 249–272. <https://doi.org/10.1007/s10546-021-00681-7> , 2022.

1078

1079 Zhu, W., Sun, J., Yang, C., Liu, M., Xu, X., and Ji, C.: How to Measure the Urban Park Cooling
1080 Island? A Perspective of Absolute and Relative Indicators Using Remote Sensing and Buffer
1081 Analysis. *Remote Sens.* *13*, 3154. <https://doi.org/10.3390/rs13163154>, 2021.

1082

1083

1084

1085

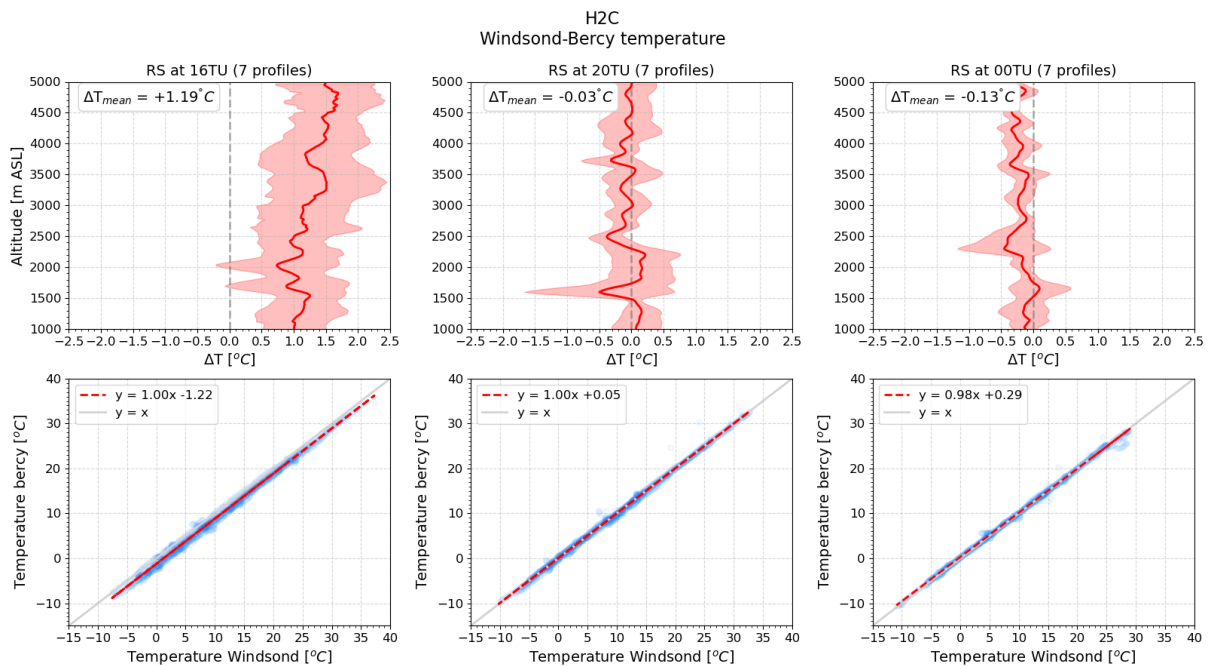
1086

1087 **Appendix A: Windsond temperature profiles**
 1088 **assessment**

1089

1090 The evaluation of the Windsond temperature profiles was conducted by comparing them with
 1091 the Vaisala RS41 temperature profiles launched at Quai de Bercy (URBAN-B site in Fig. 1)
 1092 during the SOP 2022. Data from seven IOPs were used for this evaluation, with profiles
 1093 recorded at 16:00, 20:00, and 00:00 UTC, respectively. Von Rohden et al (2022) find a
 1094 radiation bias of 0.1°C in Vaisala RS41 temperature data in the troposphere. Our comparisons
 1095 reveal an average warm bias of 1.2°C in windsond temperature profiles compared to Vaisala
 1096 RS41 values of 16 UTC profiles. No significant bias is found at 20 and 00 UTC.

1097



1098

1099 Figure A1: Assessment of windsond temperature profiles. a-c) Average temperature
 1100 differences between the Windsond and Vaisala RS-41 temperature profiles from 1000m to
 1101 5000m ASL at 16, 20 and 00 UTC respectively. d-f) Point-to-point correlations between
 1102 Windsond and Vaisala RS-41 temperatures.

1103

1104

1105